Laser noise characterization with balanced Mach-Zehnder interferometer

Kaylan Weber

Bachelorarbeit in Physik
angefertigt im Institut für Angewandte Physik

vorgelegt der
Mathematisch-Naturwissenschaftlichen Fakultät
der
Rheinischen Friedrich-Wilhelms-Universität
Bonn

July 2025

Ich versichere, dass ich diese Arbeit selbstständig verfasst und keine anderen als die angegebenen Quellen und Hilfsmittel benutzt sowie die Zitate kenntlich gemacht habe.

Bonn, ...
Datum Unterschrift

1. Gutachter: Prof. Dr. Sebastian Hofferberth
2. Gutachter: Dr. Frank Vewinger

Contents

CHAPTER 1

Introduction

Lasers have undoubtedly become one of the key instruments for modern technology and research over the past decades. Their application is widely spread and crosses over to fields like manufacturing, medicine, metrology, communications and scientific research. In the branch of physics they are heavily used in fields of laser spectroscopy and quantum technologies [1].

In cold-atom experiments, lasers are used to drive the atomic transitions for cooling of atoms and manipulation of their internal states. In the rubidium quantum optics experiment, we are coherently driving two-photon transitions between ground and high-lying Rydberg states. We realize the coherent interaction between few-photon pulses and effective two-level atoms, so called Rydberg superatoms [2], with the feature of Rabi oscillations imprinted onto the transmitted light field [3]. Rydberg superatoms are a testbed for nonlinear quantum optics [3] and can be applied as single-photon sources [4] or for performing optical quantum gates [5] [6]. The coherent interaction between few-photons and the atoms is impaired by multiple decoherence mechanisms

The most common sources include the Doppler effect arising from atomic motion [7], spontaneous emission via intermediate states, and laser intensity and frequency noise [8] [9] [10]. Frequency noise describes fluctuations of the frequency or phase of the laser on varying time scales. Therefore, it has great impact on the stability and coherence of the laser which need to be stable on the time scale of the experiment. One important time scale is the duration of a single experiment, which lies for our Rydberg experiments in the ten microsecond regime. The laser also needs to be stable on the seconds to hours timescale as data is acquired and averaged over many experiment cycles. Instabilities and flucuations on long time scales can obscure any signal in the retrieved data. The laser frequency stabilization over a wide range of time scales is realized with a feedback loop [11]. In order to characterize the quality of the laser frequency stabilization, we are interested in the laser frequency noise spectrum. In the context of our experiments, we are interested in the frequency range of 100 kHz to 10 MHz.

There are multiple methods in order to characterize frequency noise responsible for fluctuations on short timescales. One method is by using a second laser as a reference and a fast photodetector in order to obtain a beat note which can be converted to a frequency difference attributed with frequency noise. A second method is to use a Fabry-Perot cavity as a frequency reference. The side of a cavity transmission peak can convert laser frequency variations into cavity transmission changes recorded on a photodetector. The frequency calibration relies on precise knowledge of the free-spectral range of the cavity. A third method is to use an interferometer and measuring the interference of the laser beam with itself. This signal can again be converted to frequency deviations and therefore allow the characterization of the lasers noise spectrum. As opposed to the heterodyne detection, the homodyne detection using i.e. an interferometer doesn't allow for the measurement of frequency noise at low Fourier-frequencies due to the delay between the two beams being too short. The noise in these low frequency regions does not interest us as it is not of importance in the relevant experiments.

In this thesis, I have used a Mach-Zehnder interferometer for the calculation of frequency noise. The goal is to build a portable device to characterize lasers of wavelengths in the region of 780 nm to 1020 nm via their Noise Spectral Densities $S_{\nu;i}$ in $\mathrm{Hz}^2/\mathrm{Hz}$. Chapter 2 covers the theory and origin of frequency noise and its calculation. Chapter 3 describes the portable experimental setup and outline how to apply it for characterizing any given laser. Chapter 4 presents a range of different lasers types operated in our lab and their respective noise spectral densities. Furthermore, the influence of a feedback loop onto the noise spectral densities is discussed. Finally, chapter 5 gives a summary of the thesis and discusses possible upgrades and applications for the setup.

CHAPTER 2

Frequency noise theory and displacement of a Piezoelectric Actuator

2.1 Origin of Laser Frequency Noise

Laser frequency noise refers to fluctuations in the optical frequency $\nu(t)$ of the emitted light. It plays a crucial role in determining the spectral linewidth and temporal coherence of the laser. These fluctuations arise from a combination of fundamental quantum noise processes and technical (classical) noise sources. The instantaneous frequency is defined as [8]

$$\nu(t) = \frac{1}{2\pi}\frac{d\varphi}{dt} \tag{2.1}$$

Therefore changes of the phase directly influence the instantaneous frequency and the frequency noise.

2.1.1 Quantum Noise

One of the origins of frequency noise in a laser is spontaneous emission, which introduces random phase perturbations into the coherent field. Each spontaneously emitted photon adds an unpredictable phase shift, leading to frequency fluctuations over time. Another effect is related to linear losses in the laser medium. These two effects contribute equally to phase diffusion and to a lower bound on the linewidth of the laser [12], known as the Schawlow–Townes linewidth [13]:

$$\Delta\nu_{\mathrm{laser}} = \frac{4\pi\, h\nu\, \left(\Delta\nu_{\mathrm{c}}\right)^2}{P} \tag{2.2}$$

where $h\nu$ is the photon energy, P is the output power, and $\Delta\nu_{\mathrm{c}}$ is the linewidth of the laser cavity. Both linewidths are interpreted as half width at half-maximum.

2.1.2 Technical Noise Sources

In addition to quantum-limited noise, practical lasers are also subject to several technical noise sources that contribute to frequency noise:

Variations in temperature can affect the refractive index and physical length of the laser cavity, thereby modulating the optical path length and frequency [14].

Also, acoustic and seismic disturbances can mechanically perturb cavity dimensions or mirror positions, particularly in external cavity diode lasers [15].

2.1.3 Frequency Noise and Linewidth

The spectral linewidth of a laser is directly related to its frequency noise power spectral density $S_\nu(f)$. A flat $S_{\nu;\,\mathrm{white}}(f)$ corresponds to white frequency noise, $1/f$ noise leads to $S_{\nu;\,1/f}(f) \propto \frac{1}{f^\alpha}$. The origin of $1/f$ noise is not entirely understood [16].

The frequency noise of semiconductor lasers is often a lot higher than that of other solid-state lasers. One cause for this is a higher spontaneous emission factor due to reabsorption in the semiconductor. Also, there are strong amplitude-to-phase coupling effects which can strongly increase the linewidth and frequency noise [17]. Fluctuations in the amounts of charge carriers (conduction electrons or valence band holes) can lead to excess $1/f$ noise. [18]

2.1.4 Laser Locking

The principle of laser locking is based on a feedback loop to actively tune the phase or frequency of the laser [19]. In the following, the Pound-Drever-Hall effect will be explained [20] as one possible method for laser locking as it is performed on the lasers that are measured in this thesis.

First, the frequency of the laser is measured with a photodetector using a Fabry-Perot cavity. The signal measured is fed back via a feedback loop to actively adjust the frequency of the laser. For this a PID-controller is used, which in weighable parts uses proportional (P), integrated (I) and differentiated (D) parts of the signal in order to create an error signal. The different parts are tuned in order to maximize the suppression of frequency fluctuations.

2.2 Displacement of a Piezoelectric Actuator Under Applied Voltage

2.2.1 Theory

Piezoelectric actuators operate based on the inverse piezoelectric effect, where an applied electric field causes a mechanical deformation of the piezoelectric material. This is due to the alignment and stretching of internal electric dipoles within the crystal structure. The resulting strain produces a displacement approximately proportional to the applied voltage [21].

Linear Displacement Approximation

In the ideal case, the displacement ΔL is modeled linearly:

$$\Delta L = d_{33} \cdot U \tag{2.3}$$

where d_{33} is the piezoelectric coefficient, and U is the applied voltage.

Hysteresis Effect

In practice, the voltage-displacement relationship of piezoelectric actuators exhibits a hysteresis. This means that the path of increasing voltage differs from the path of decreasing voltage, resulting in a loop-shaped curve in the displacement vs. voltage plot.

Hysteresis occurs because the internal dipoles in the piezo material do not respond instantaneously or uniformly to changes in the electric field. Instead, they experience friction-like resistance and memory effects. This behavior is similar to magnetic hysteresis in ferromagnets.

2.3 Measurement of frequency noise

To characterize the phase and frequency noise of a laser it is necessary to transform from the hundreds of THz frequency of the electromagnetic wave to a frequency range that is detectable by standard electronics. Therefore, interferometry is used to access the laser noise.

In this case, a Mach-Zehnder interferometer with unbalanced arm lengths was used. Its setup can be seen in 2.1. Fluctuations in the frequency leads to changes in the phase between the short and long arm. We measure the noise spectrum of the interference between the two time-delayed signals.

The two outputs A and B can be detected by a balanced photodetector. The light in the two arms has a phase difference of exactly π due to different paths the light follows through the mirrors and beam splitters on the way to the two detectors [22]. This is compensated by subtracting the two signals from A and B when measuring an interference signal, which effectively leads to a doubling of the amplitude and removing any constant offset not related to interference in the arms.

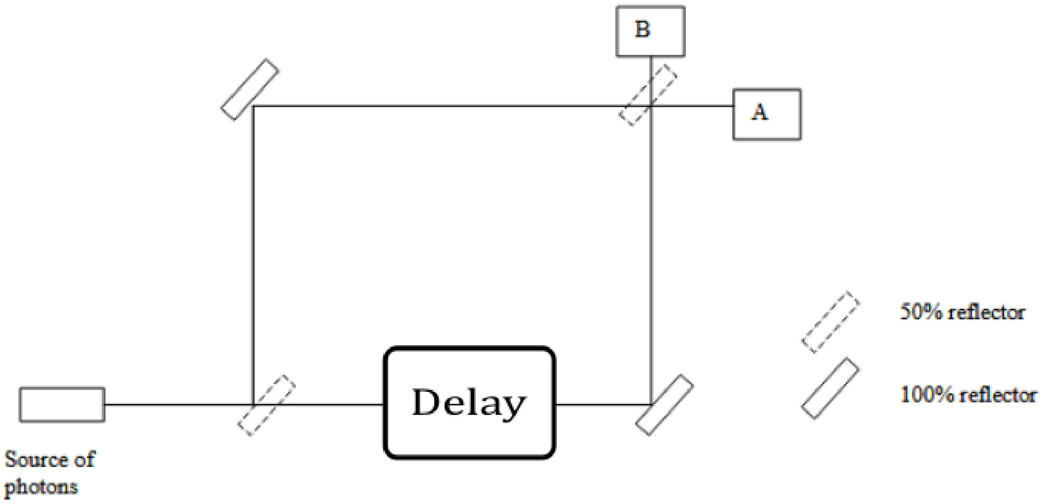

Figure 2.1: Sketch of a Mach-Zehnder interferometer based off of [22]. The light is split equally into the short arm (left) and long arm (right) in which the light is delayed before it is recombined with the short arm. The light as detected at A and B.

2.4 Calculation of frequency noise

The goal is to convert a change in phase between the beams of the two arms into a frequency difference. This allows us to calculate the frequency noise.

In the used setup the electric field of the two beams has the following form:

$$E_{1,2}(t) = E_{1,2} \cdot \sin\left(2\pi\nu \cdot t + \varphi_{1,2}\right) \tag{2.4}$$

There is an additional phase shift of π for the light being fed into the lower input of the photodetector in 3.1.

By overlapping the two beams we measure the following intensity at the individual inputs of the photodetector:

$$\begin{aligned} I \sim \left\langle E(t)^2 \right\rangle = \Big\langle & E_1^2 \cdot \sin^2(2\pi\nu \cdot t + \varphi_1) + E_2^2 \cdot \sin^2(2\pi\nu \cdot t + \varphi_2) \\ & + E_1 E_2 \cdot \left(\cos\left(\varphi_2 - \varphi_1\right) - \cos\left(4\pi\nu \cdot t + \varphi_1 + \varphi_2\right)\right)\Big\rangle \end{aligned}$$

Since the photodetector can't resolve the terms oscillating with frequencies as high as those of the used light we get an interference intensity of the following form:

$$I = \frac{E_1^2 + E_2^2}{2} + E_1 E_2 \cos(\Delta\varphi) \tag{2.5}$$

The frequency of the beam is not constant and has a time-dependent part $\Delta\nu$ which is summed onto the constant part.

$$\nu(t) = \nu_0 + \Delta\nu(t) \tag{2.6}$$

$\Delta\nu$ is the frequency noise we want to measure. This change in frequency over time leads to the beam in the long arm acquiring a phase over the delayed time τ compared to the beam in the short arm. The change in phase over a time interval dt in which we consider the frequency $\nu(t)$ to be constant is given by $d(\Delta\varphi) = 2\pi\nu(t)dt$. Summing over the entire delay time τ we get

$$\begin{aligned} \Delta\varphi(t) &= 2\pi \int_{t-\tau}^{t} \nu(t')dt' + \varphi_0 = 2\pi \int_{t-\tau}^{t} \Delta\nu(t')dt' + 2\pi\nu_0\tau + \varphi_0 \\ &= 2\pi \int_{t-\tau}^{t} \Delta\nu(t')dt' + \varphi_0' \end{aligned} \tag{2.7}$$

Here the constant terms resulting from the difference in path length of the two arms (φ_0) and the constant part resulting from the constant frequency in (2.6) are summarized into a constant phase shift φ_0'. We are only interested in changes of the phase.

In the following the frequency noise $\Delta\nu(t)$ is described as a superposition of oscillations with frequencies f_i and random phases $\varphi_{f,i}$ [23]

$$\Delta\nu(t) = \sum_i \sqrt{2S_{\nu,i}\Delta f} \cdot \cos\left(2\pi f_i \cdot t + \varphi_{f,i}\right) \tag{2.8}$$

Here $\Delta f = f_{i+1} - f_i$ is the difference between two frequencies and $S_{\nu,i}$ is the spectral power of the i-th frequency component.
Using (2.7) we obtain the following phase shift

$$\begin{aligned}\Delta\varphi(t) &= 2\pi \sum_i \sqrt{2S_{\nu;i}\,\Delta f} \int_{t-\tau}^{t} \cos\left(2\pi f_i \cdot t' + \varphi_{f;i}\right) \mathrm{d}t' \\ &= 2\pi \sum_i \sqrt{2S_{\nu;i}\,\Delta f} \left[\frac{1}{2\pi f_i} \sin\left(2\pi f_i \cdot t' + \varphi_{f;i}\right)\right]_{t-\tau}^{t} + \varphi_0' \\ &= \sum_i \sqrt{2S_{\nu;i}\,\Delta f} \cdot \frac{2}{f_i} \sin(\pi f_i \tau) \cos\left(2\pi f_i \cdot t - \pi f_i \tau + \varphi_{f;i}\right) + \varphi_0' \\ &= \sum_i \sqrt{2S_{\nu;i}\,\Delta f} \cdot \frac{2\sin(\pi f_i \tau)}{f_i} \cos\left(2\pi f_i \cdot t + \varphi_{f;i}'\right) + \varphi_0' \end{aligned} \tag{2.9}$$

Again we add up all the constant phase contributions into φ_0'. This phase is affected by changes in the path difference between the two arms. This difference is very sensitive to temperature changes due minimal expansion of the instruments which leads to changes in the path lengths of the two arms. We keep this phase constant over time by using the feedback loop with the piezo mirror.

The square root $\sqrt{2S_{\nu,i}\Delta f}$ term describes the amplitude of each oscillation and is a measure for the deviation from the frequency ν_0 with oscillation frequency f_i.

The second term $\frac{2\sin(\pi f_i \tau)}{f_i}$ is a suppression term that describes destructive interference between different noise components.

The cosine term $\cos\left(2\pi f_i \cdot t + \varphi_{f;i}'\right)$ describes the oscillation around of the laser frequency with the oscillation frequency f_i.

Plugging $\Delta\varphi$ into (2.5) we have obtained a direct relationship between the measured intensity at the balanced photodetector and the frequency noise spectrum characterized by $S_{\nu,i}$ and f_i.

With the inverse function

$$\Delta\varphi = \arccos\left(\frac{U_{\text{Diode}} - U_{\text{offset}}}{U_0}\right) - \varphi_0' \tag{2.10}$$

we obtain the phase difference from the measured diode signal.
Using the PID Box, we lock the signal around 0 V. Since the diode signal ideally has an offset of about 0 V we ensure that the signal is locked at the steepest slope as seen in 2.2. Since the frequency noise only causes minimal deviation of the signal from the locked point we can approximate the Voltage-Phase relationship as a linear function.

$$\left.\frac{dU_{\text{Diode}}}{d(\Delta\varphi)}\right|_{\Delta\varphi=\varphi_{\text{lock}}} \approx \left.\frac{\Delta U_{\text{Diode}}}{\Delta(\Delta\varphi)}\right|_{\Delta\varphi=\varphi_{\text{lock}}} \tag{2.11}$$

φ_{lock} is the relative phase where the signal is locked. This is obtained by applying the inverse function (2.10) to the lock voltage U_{lock}.

$$\varphi_{\text{lock}} = U_{\text{Diode}}^{-1}\left(U_{\text{lock}}\right) \tag{2.12}$$

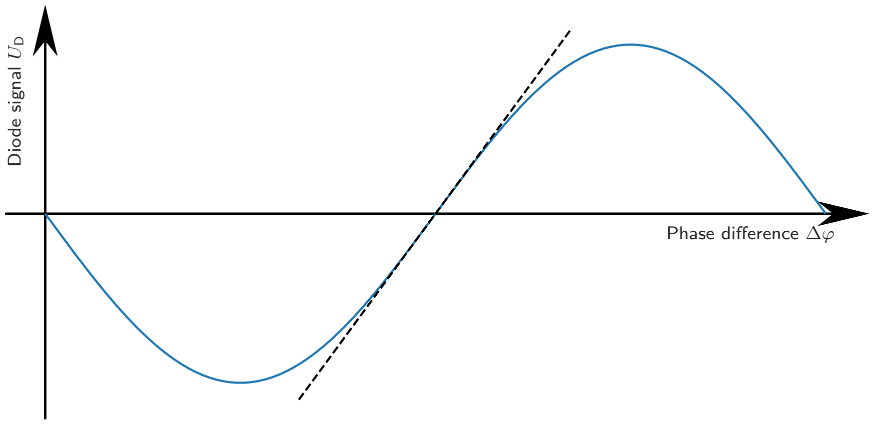

Figure 2.2: Locking the phase between the two arms to the most sensitive point i.e. the point with the steepest slope denoted by the dashed line.

Taking the first derivative of (3.5)

$$\left.\frac{dU_\mathrm{Diode}}{d(\Delta\varphi)}\right|_{\Delta\varphi=\varphi_\mathrm{lock}} = -U_0 \cdot \sin\left(\varphi_\mathrm{lock} + \varphi_0'\right) \tag{2.13}$$

one can calculate the phase difference from the diode signal

$$\Delta\varphi - \varphi_\mathrm{lock} = \left(\left.\frac{dU_\mathrm{Diode}}{d(\Delta\varphi)}\right|_{\Delta\varphi=\varphi_\mathrm{lock}}\right)^{-1} \cdot \left(U_\mathrm{Diode} - U_\mathrm{lock}\right) \tag{2.14}$$

To obtain the power spectrum $S_{\nu,i}$ one first performs a Fourier transform to the measured diode voltage to obtain the power spectrum $S_{U,i}$ in $\frac{\mathrm{V}^2}{\mathrm{Hz}}$.

$$U_\mathrm{Diode}(t) = \sum_i \sqrt{2S_{U;i}\,\Delta f}\ \cos\left(2\pi f_i \cdot t + \varphi'_{f;i}\right) + U_\mathrm{DC} \tag{2.15}$$

With the constant offset U_DC which is included due to an average being subtracted from the trace before performing the Fourier transform.

Plugging this into the right side of (2.14) and using the expression (2.9) one obtains

$$\Delta\varphi - \varphi_{\text{lock}} = \sum_i \sqrt{2S_{\nu;i}\,\Delta f} \cdot \frac{\sin(\pi f_i \tau)}{f_i} \cos\left(2\pi f_i \cdot t + \varphi'_{f;i}\right) + \varphi'_0 - \varphi_{\text{lock}} \tag{2.16}$$

$$\begin{aligned} &= \left(\left.\frac{dU_{\text{Diode}}}{d(\Delta\varphi)}\right|_{\Delta\varphi=\varphi_{\text{lock}}} \right)^{-1} \cdot \sum_i \sqrt{2S_{U;i}\,\Delta f} \cos\left(2\pi f_i \cdot t + \varphi'_{f;i}\right) \\ &\quad + \underbrace{\left(\left.\frac{dU_{\text{Diode}}}{d(\Delta\varphi)}\right|_{\Delta\varphi=\varphi_{\text{lock}}} \right)^{-1} \cdot (U_{\text{DC}} - U_{\text{lock}})}_{\varphi'_0 - \varphi_{\text{lock}}} \end{aligned} \tag{2.17}$$

The constant term of the Voltage trace U_{DC} translates to φ'_0 via (2.14). Comparing the two expressions for each frequency component one obtains

$$\sqrt{2S_{\nu;i}\,\Delta f} \cdot \frac{2\sin(\pi f_i \tau)}{f_i} = \left(\left.\frac{dU_{\text{Diode}}}{d(\Delta\varphi)}\right|_{\Delta\varphi=\varphi_{\text{lock}}} \right)^{-1} \cdot \sqrt{2S_{U;i}\,\Delta f} \tag{2.18}$$

$$\Leftrightarrow \qquad S_{\nu;i} = \left(\left.\frac{dU_{\text{Diode}}}{d(\Delta\varphi)}\right|_{\Delta\varphi=\varphi_{\text{lock}}} \right)^{-2} \left(\frac{f_i}{2\sin(\pi f_i \tau)} \right)^2 \cdot S_{U;i} \tag{2.19}$$

This allows the translation of power spectral densities $S_{U;i}$ into noise spectral densities $S_{\nu;i}$.

$$S_{U;i} = s(f_i) \cdot S_{\nu;i} \tag{2.20}$$

$s(f_i) = \left(\left.\frac{dU_{\text{Diode}}}{d(\Delta\varphi)}\right|_{\Delta\varphi=\varphi_{\text{lock}}} \right)^2 \left(\frac{2\sin(\pi f_i \tau)}{f_i} \right)^2$ is the Fourier-frequency-dependent sensitivity of the measurement [8]. It describes how the frequency fluctuations $\Delta\nu(t)$ translate to the measured voltage $\Delta U_{\text{Diode}}(t)$. A higher sensitivity increases the accuracy of the performed measurements.

2.5 Sensitivity

The Fourier-frequency-dependent sensitivity can alternatively be written as

$$s(f_i) = \underbrace{4\pi^2\tau^2\left(\frac{dU_{\mathrm{Diode}}}{d(\Delta\varphi)}\bigg|_{\Delta\varphi=\varphi_{\mathrm{lock}}}\right)^2}_{s_0} \cdot \left(\frac{\sin(\pi\tau f_i)}{\pi\tau f_i}\right)^2 \tag{2.21}$$

where we have seperated the sensitivity into a constant factor s_0 and a Fourier-frequency-dependant factor that is normalized.

$$\left(\frac{\sin(\pi\tau f_i)}{\pi\tau f_i}\right)^2 \tag{2.22}$$

This Fourier-frequency-dependency of the sensitivity is shown in 2.3

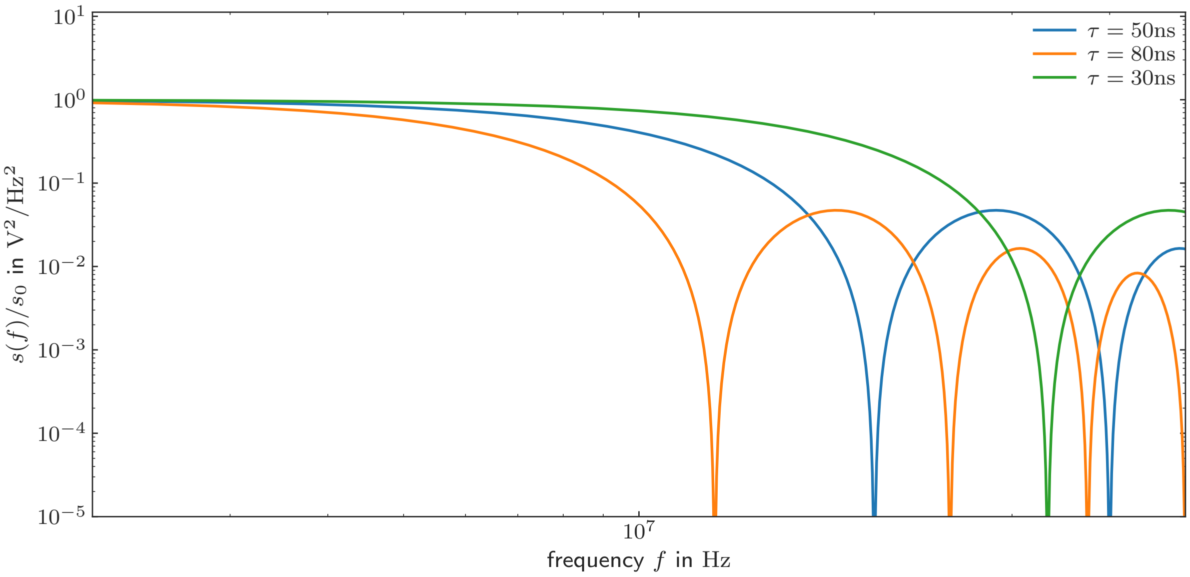

Figure 2.3: Fourier-frequency-dependency of sensitivity $s(f)$

It can be seen that this factor is approximately equal to one up to frequencies of approximately 10 MHz for $\tau = 50$ ns, which is approximately the chosen value for our setup. Therefore, the Fourier-frequency dependency of the sensitivity only becomes relative for frequencies above 10 Mhz. The sensitivity is mainly determined by s_0 for the bigger part of the spectrum i.e. frequencies up to 10 Mhz.

2.6 Noise suppression

When observing the measured power spectral densities $S_{U;i}$, calculated either by performing a Fourier transform of the measured oscilloscope trace or by the spectrum analyzer directly, one observes dips in the spectrum starting at around 10 MHz. These are caused by destructive interference between different noise components described by the suppression term $\frac{2\sin(\pi f_i \tau)}{f_i}$.

This term includes the parameter τ which is given as the difference between the times of the beams of the short and long arm needed to reach the diode.

$$\tau = \frac{\Delta s}{c} + \frac{l \cdot n}{c} \tag{2.23}$$

Where Δs is the path difference for the unguided part of the beams. l is the length of the fiber and n the refraction index of the fiber.
A precise calculation of τ is not possible due to errors arising when measuring the distances traveled by the beams within the setup. Thus, the idea is to perform a fit to the uncorrected spectrum to gain τ as a fit parameter.

The corrected noise spectrum $S_{\nu;i}$ can be approximated as flicker noise of the following form

$$S_{\nu;i} = A' \frac{1}{f^{\alpha}} + B' \tag{2.24}$$

where $0 < \alpha < 2$ and A' determine the shape of the noise and B' accounts for flat (white) frequency noise and remaining background noise not eliminated by the background measurement.

Substituting this into the conversion of the power spectrum to the noise spectrum (2.19)

$$\begin{aligned} A' \frac{1}{f^{\alpha}} + B' &= \left(\left. \frac{dU_{\text{Diode}}}{d(\Delta\varphi)} \right|_{\Delta\varphi=\varphi_{\text{lock}}} \right)^{-2} \left(\frac{f}{2\sin(\pi f \tau)} \right)^2 \cdot S_{U;i} \\ \Leftrightarrow \quad \underbrace{2 \left(\left. \frac{dU_{\text{Diode}}}{d(\Delta\varphi)} \right|_{\Delta\varphi=\varphi_{\text{lock}}} \right)^{2} A'}_{=A} \frac{1}{f^{\alpha}} + \underbrace{2 \left(\left. \frac{dU_{\text{Diode}}}{d(\Delta\varphi)} \right|_{\Delta\varphi=\varphi_{\text{lock}}} \right)^{2} B'}_{=B} &= \left(\frac{f}{\sin(\pi f \tau)} \right)^2 \cdot S_{U;i} \\ \Leftrightarrow \qquad S_{U;i} &= \left(\frac{\sin(\pi f \tau)}{f} \right)^2 \left(A \frac{1}{f^{\alpha}} + B \right) \end{aligned} \tag{2.25}$$

We now have a function to describe the uncorrected power spectrum with τ as a fit parameter.

The suppression term $\left(\frac{\sin(\pi \tau f_i)}{f_i}\right)^2$ has the same form as the Fourier-frequency-dependent sensitivity $s(f)/s_0$ shown in 2.3 for different values of τ. It is simply multiplied by the constant factor of $4\pi^2\tau^2$. Therefore, the measured power spectrum densities $S_{U;i}$ are approximately proportional to the noise spectral densities $S_{\nu;i}$ up to the 10 MHz range. For higher frequencies, suppression dips arise in the measured power spectrum $S_{U;i}$ similar to the dips seen for the sensitivity.

CHAPTER 3

Setup and how-to

3.1 Setup

As mentioned in the previous chapter, a Mach-Zehnder interferometer with unbalanced arm lengths is built in order to measure frequency noise. In this case the delay is caused by passing the light through a fiber of the length of 10 m in the long arm.

This chapter first discusses the setup of the interferometer and how armlength is stabilized. Because the setup described in this thesis is meant to be portable some details about the alignment procedure are given here for future use. Finally, the details of noise measurements are discussed.

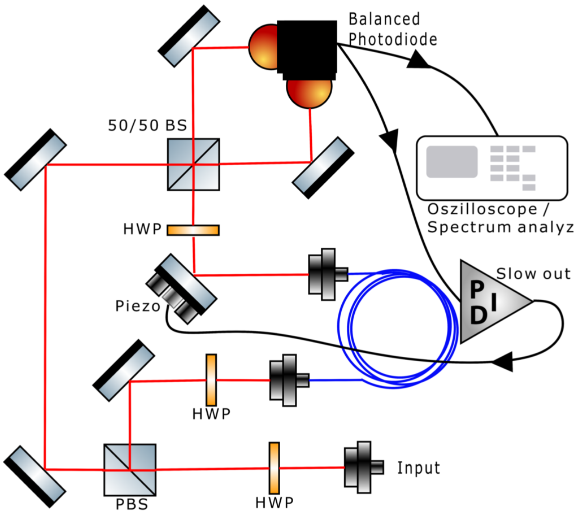

Figure 3.1: Setup of balanced Mach-Zehnder interferometer including oscilloscope to measure the trace and PID controller to lock the phase between the two arms

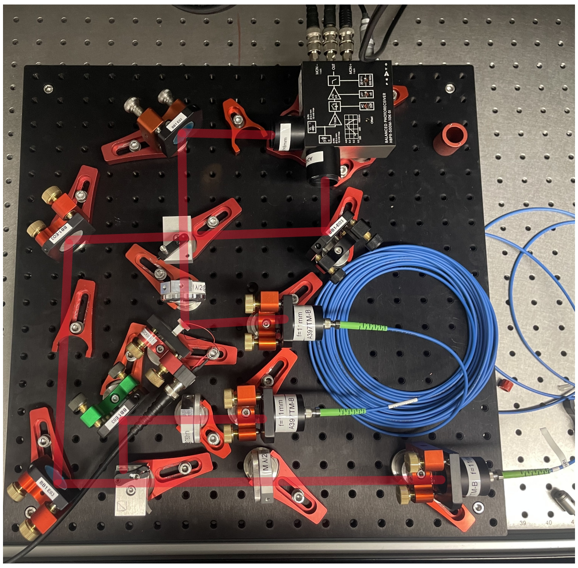

Figure 3.2: Picture of implemented setup

Figure 3.1 shows the Mach-Zehnder interferometer used to characterize laser noise. The laser to be characterized must be fiber coupled. The fiber coupled signal enters the noise measurement setup through the input fiber. The light from the fiber incoupler passes through a Half-Wave Plate (HWP) before being split by a Polarising Beam Splitter (PBS). This HWP ensures that the light is equally distributed into the short and long arm of the setup. The short arm on the left side of the figure simply redirects the light to a 50/50 Beam Splitter (50/50 BS). In the long arm, the light passes through another HWP before being coupled into a polarization maintaining fiber (blue). The fiber is responsible for delaying the light in the long arm. The fiber is 10 m long, corresponding to a delay of 49 ns. This second HWP is used to match the polarization of the light to the polarization maintaining axis of the delay-fiber and thereby ensure resistance to polarization drifts in the fiber. After the outcoupling, the light is reflected by the piezo mirror. The piezo mirror is used to minimally displace the beam in the long arm if necessary to stabilize the interferometer path length, and will be discussed in more detail later. After the piezo, the light in the long arm passes through another HWP in order to match the polarization of the light in the two arms. A second 50/50 BS is used to recombine the two arms. The two outputs from the BS are detected by a balanced photo detector. The light in the two arms has a phase difference of exactly π due to different paths the light follows through the mirrors and PBSs on the way to the two detectors [22]. The balanced photodetector [1] gives as its output the difference between the two detected signals. The resulting difference is used as the output signal of the laser noise detection setup.

All the used optics in the setup are b-coated, meaning the setup allows usage across the near infrared spectrum (650 nm to 1050 nm). However, the HWPs need to be exchanged for different wavelengths as they work only in very narrow ranges.

Additionally, a box was built around the setup that prevents airflow that can cause vibrations. The setup is portable and has a footprint of 45 × 45 cm.

---

[1] FEMTO Messtechnik GmbH HBPR-500M-10K-SI-FST High-Speed Balanced Photoreceiver

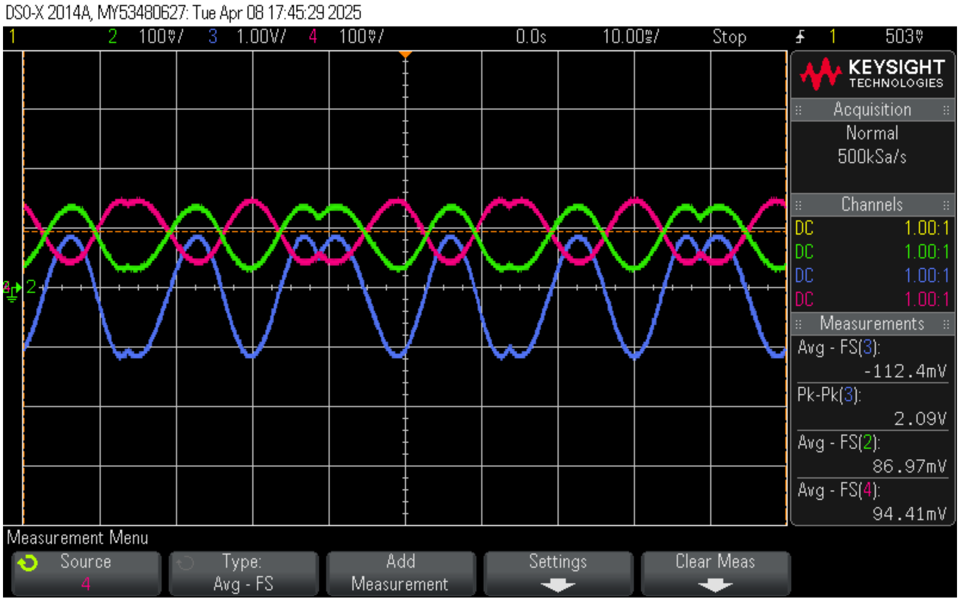

Avg - FS(3): -112.4mV
Pk-Pk(3): 2.09V
Avg - FS(2): 86.97mV
Avg - FS(4): 94.41mV

Figure 3.3: Balanced photodetector signal when applying a ramp signal. The green and pink signals show the individual outputs of the diodes. The phase difference of π is visible and the subtracted signal is shown in blue.

The two photodiodes in the balanced photo detector detect the interference between the long and short arm. The interference depends on the relative path length. By moving the position of the piezo mirror on the lengthscale of the wavelength we see the sinusoidal interference pattern. The piezo takes input voltages of up to 120 V.

Figure 3.3 shows the output signal from the photodetector when applying a ramp signal to the piezo. Here, a 20 V peak-to-peak value ranging from −10 V to +10 V with a frequency of 20 Hz was used.

In order to extract noise on the laser the position of the piezo is controlled such that the phase difference between the field in the two different arms ($\Delta\varphi$ in equation (2.5)), and hence the voltage output of the photo detector is kept constant. Figure 3.1 shows the interferometer setup and how a feedback loop is used to control the piezo position to maintain a specified photo detector voltage and hence phase difference between the arms. To stabilize the piezo position a homebuilt PID-controller is used. Details of the PID controller are for instance given in [24]. The photo detector difference output voltage is used as the signal to be stabilized and is therefore the input to the PID controller. The PID controller also has a reference input where the lockpoint can be specified. In this case the lockpoint is set to 0 V by grounding the reference input, corresponding to locking the interferometer where the intensities at the two photodiodes are equal.

The PID controller has two different outputs, a slow and a fast one. In this case only the slow output is used, since a fast stabilization would also suppress the laser noise that we want to measure. The slow output can suppress noise up to 100 Hz [25].

The signal from the balanced photodetector is not only used to stabilize the interferometer arm length, but also to access the actual noise spectrum. For this purpose, the signal is split with a T-piece and we feed the diode signal to a high resolution oscilloscope [2] or a spectrum analyzer.

In the next section we discuss the linearity of the piezo response and how the piezo response can also be used as a way of accessing phase noise.

---

[2] TELEDYNE LECROY WavePro 404 HD

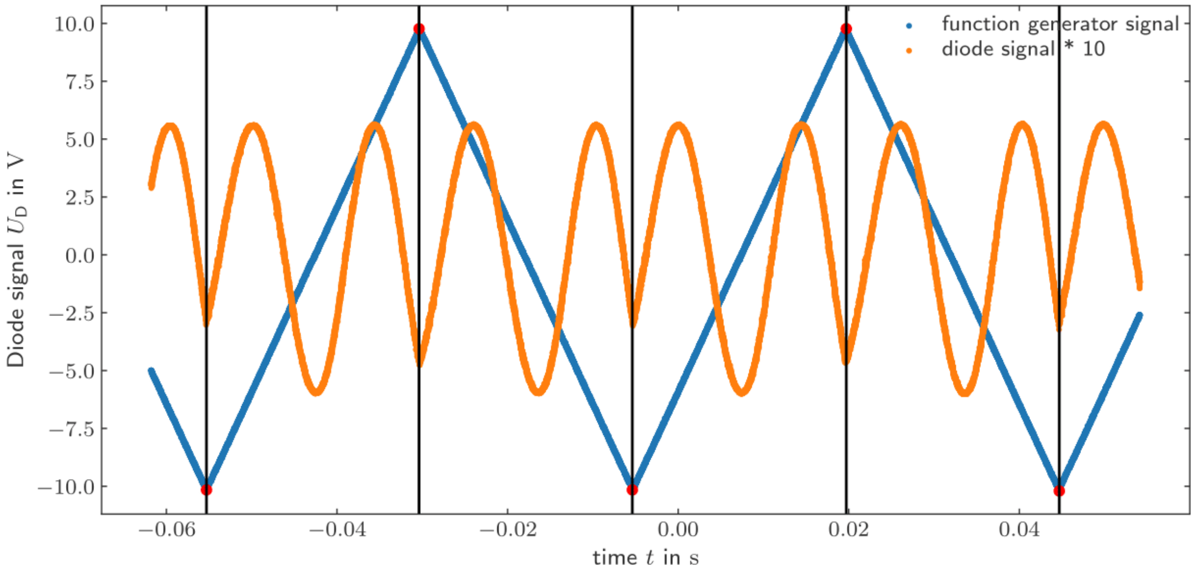

Figure 3.4: Trace of a calibration measurement including the photodetector signal and corresponding ramp signal being applied to the piezo mirror. The discontinuities are shown by the red points by which the trace is cut into parts for a rising or falling ramp

3.2 Calibration measurement

In this thesis, the laser noise is measured with the photo detector signal, but as shown in Figure 3.3 the interference signal is sinusoidal. To get access to the magnitude of different noise components, it is necessary to perform a calibration that maps a photo detector voltage to a phase difference between the two interferometer arms.

In the following it is discussed how a calibration is performed. The linearity of the used piezo mirror is also investigated.

The calibration measurement is performed by ramping the voltage applied to the piezo as shown in 3.1. The piezo ramp voltage and the resulting photodetector signal are shown in Figure 3.4. A linear function is fitted to the ramp signal for each rising or falling ramp. In each interval the x-axis of the diode signal is transformed from time t in seconds to the piezo input voltage in volts. Figure 3.5 shows the photo detector signal plotted as a function of piezo voltage for one piezo ramp. It is apparent from the figure that the diode signal has a different form whether we are on a rising or falling slope. This difference comes from hysteresis of the piezo. In the following section we characterize this hysteresis.

3.2.1 Measured Displacement of Piezoelectric Actuator

Comparing the two different curves shown in figure 3.5, which shows the photodetector voltage measured for a rising and a falling voltage respectively, one sees that the displacement of the piezo shows a nonlinear behavior. For a piezo with a perfectly linear response, one would expect a signal described by

$$U_{\text{Diode}}(\Delta\varphi) = U_0 \cdot \cos(\Delta\varphi) + U_{\text{offset}} \tag{3.1}$$

where $\Delta\varphi$ behaves linearly with respect to the piezo input voltage U.

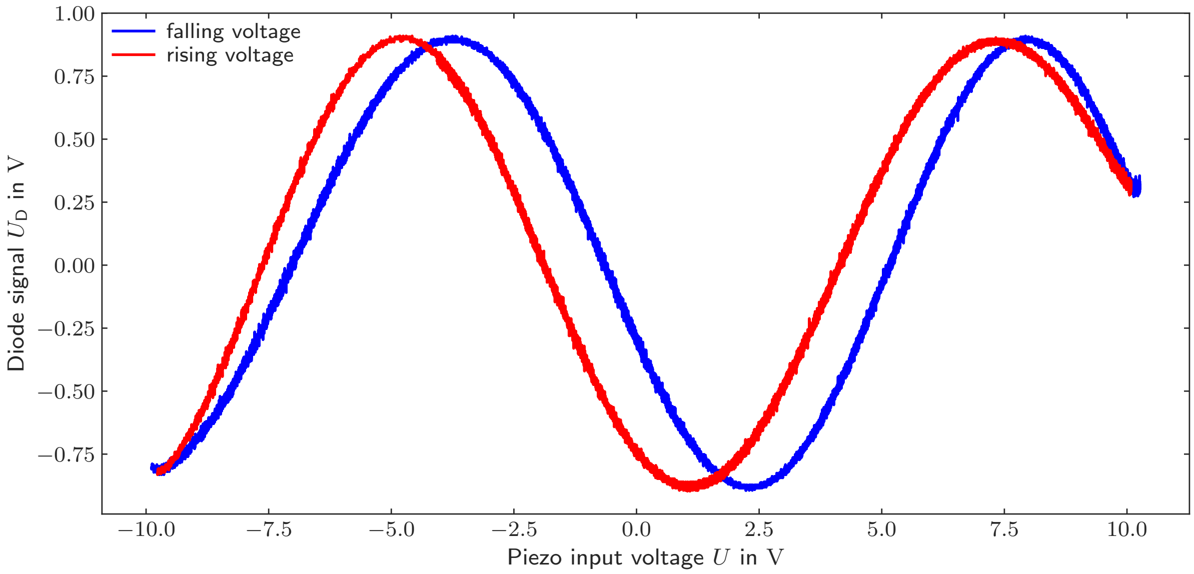

Figure 3.5: Diode signal with respect to the piezo input voltage as a rising or falling ramp

However, from the hysteresis shown in figure 3.5 it is clear that the argument of the cosine in (3.1) is not linear in applied voltage.

To verify this, we extract the argument by isolating the phase difference

$$\Delta\varphi = \arccos\left(\frac{U_{\text{Diode}} - U_{\text{offset}}}{U_0}\right) \tag{3.2}$$

U_0 and U_{offset} is gained by performing a cosine fit with a linear argument of $\Delta\varphi = a \cdot U_{\text{Diode}} + b$ to the sinusoidal diode signals seen in 3.5.

The phase $\Delta\varphi$ is calculated using equation (3.2). The result is seen in 3.6(a).

The function $\arccos(\cos(x))$ is also illustrated. Here $x = A \cdot U + B$ is simply a linear argument that represents the case of a linear displacement of the piezo with respect to the input voltage U. It is fitted to the measured phase difference, which is not linear. From the figure one can see that the arccos function has discontinuities when $\Delta\varphi = \pi$. The ragged edges and missing of data points between the discontinuities are due to the measured signal exceeding the calculated amplitude.

The unwrapped relative phase as a function of piezo voltage can be seen in 3.6(b). The relative phase difference extracted from the measured data has a phase offset for zero applied voltage to the piezo. This is to be expected as the relative phase between the interferometer arms for a given piezo position is determined by the interferometer construction and by the temperature at the time of measurement.

Nevertheless, figure 3.6(b) shows a clear hysteresis curve.

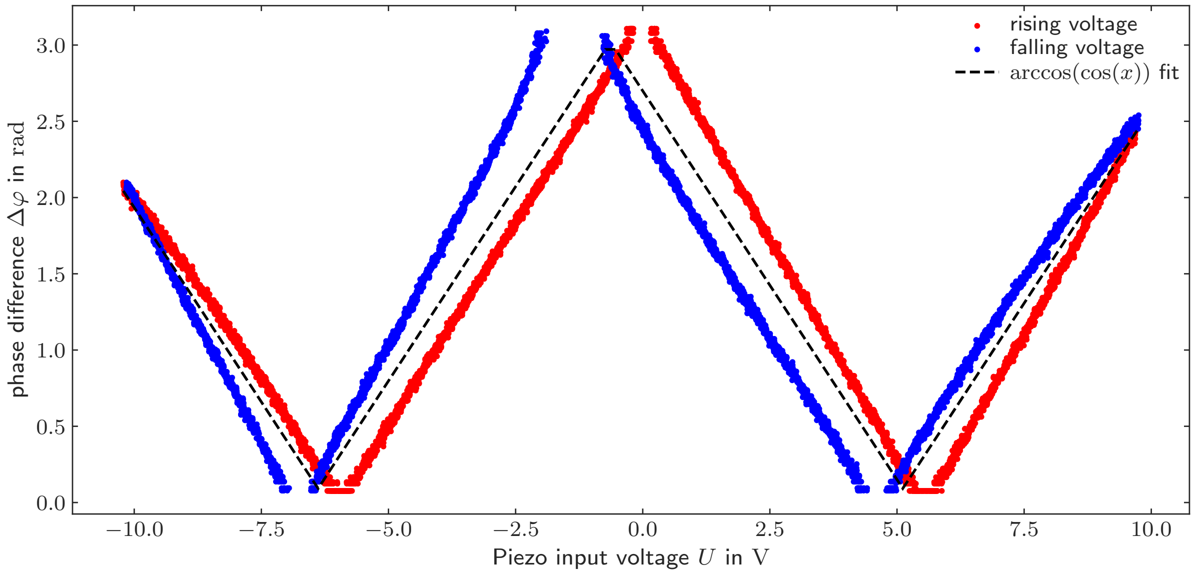

(a) uncorrected hysteresis curve. The function of arccos (cos (x)) is also illustrated as a fit to the uncorrected curve

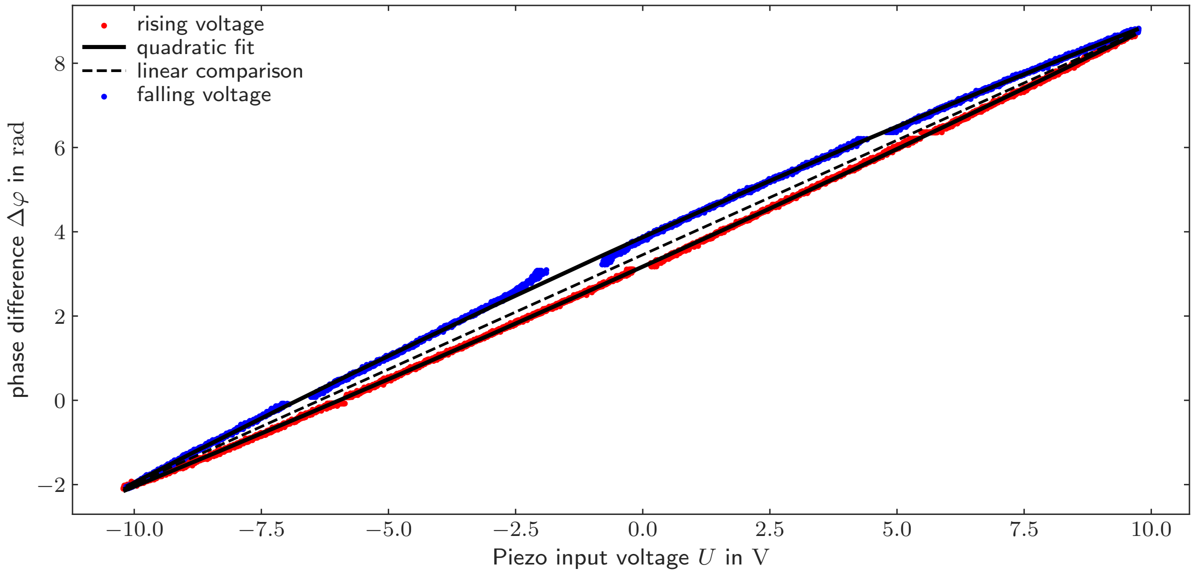

(b) corrected hysteresis curve with a quadratic fit and linear curve for comparison

Figure 3.6: Piezo phase difference with respect to the applied voltage. The top curve is calculated directly from the measured diode signal. The bottom hysteresis curve includes the correction of a continuous increase of the phase difference when increasing the voltage.

While the piezo position is not linear in applied voltage for the fast scans used in this chapter, the relative phase between the two piezo arms must directly proportional to the piezo displacement Δd. The relation is described by

$$\Delta\varphi = \frac{2\pi}{\lambda}\Delta d \tag{3.3}$$

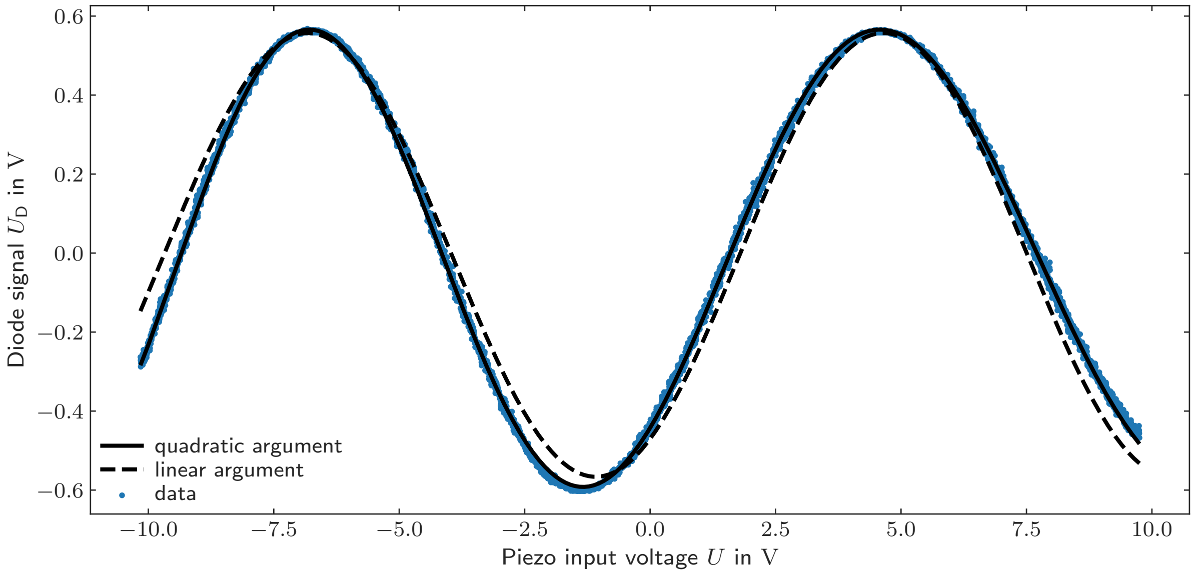

Figure 3.7: Calibration measurement with a cosine fit with a quadratic argument in the cosine (accounting for hysteresis) and with a linear argument for comparison

From this relation we can use the photodetector signal to deduce how the piezo displacement depends on applied voltage. To do this, we find a function that fits the hysteresis curves shown in figure 3.6(b). As seen in 3.6(b) a quadratic function approximates the hysteresis curve very well.

With this information we use a quadratic function in the argument of the cosine to fit a function to the photodetector signal. As seen in figure 3.7, this produces a very good fit.

It was shown that the piezo follows a hysteresis curve that can be well approximated by a quadratic function. This information is used in the context of this thesis to improve the quality of the fits used in the calibration measurement to better approximate the slope of the Diode signal function with respect to the phase difference. This slope is later used for the conversion of changes in the diode signal to changes in the phase, which are used to calculate the frequency noise spectrum.

3.2.2 Using the calibration measurement to calculate phase fluctuations

For the calibration measurement a dataset as shown in figure 3.4 is collected. The data is segmented and the x axis is converted from time to the piezo input voltage given by the ramp as seen in 3.5. For each curve a fit with the following function is performed to the diode signal

$$U_\mathrm{Diode}(U_\mathrm{P}) = U_0 \cdot \cos\left(B \cdot U_\mathrm{P}^2 + C \cdot U_\mathrm{P} + \varphi_0'\right) + U_\mathrm{offset} \tag{3.4}$$

With (3.1) one can write the diode signal as a function of the phase difference.

$$U_\mathrm{Diode}(\Delta\varphi) = U_0 \cdot \cos\left(\Delta\varphi + \varphi_0'\right) + U_\mathrm{offset} \tag{3.5}$$

We use the amplitude U_0, the phase offset φ_0' and the voltage offset U_{offset} from the performed fit. All of these values are averaged over all the fits performed in the seperated intervals seen in 3.4.

The fact that the piezo follows a hysteresis displacement curve, and we get two different fit functions for the rising and falling ramps as seen in 3.5, does not have an effect on the calculation of the phase difference. This is due to the piezo being locked to a certain phase difference. The only change of the diode signal arises from the change in frequency of the light. Since there are no changes to the piezo input voltage the diode signal follows a cosine wave with respect to the change in phase difference arising from frequency fluctuations.

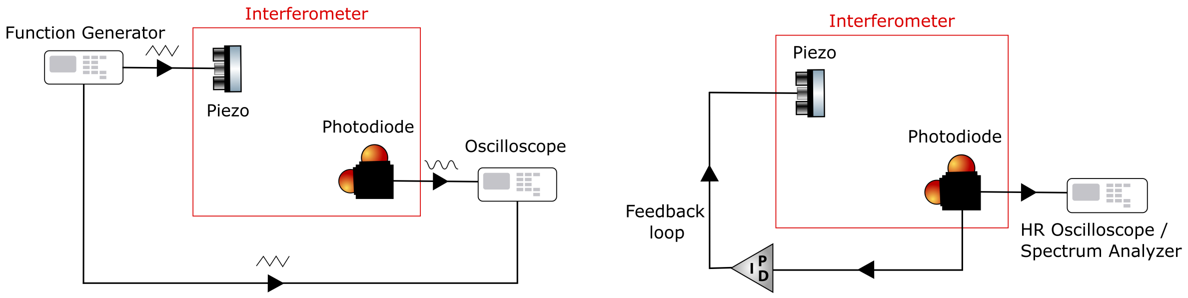

(a) Calibration measurement (b) Noise measurement

Figure 3.8: Sketches of the measurement setup

3.3 Measurements

In order to successfully determine the frequency noise of a given laser one needs to perform three measurements.

1. Calibration measurement
2. Background measurement
3. Noise measurement

In the following, the different measurements are described in a step-by-step manner. The purpose of this description is to make the interferometer usable for others who need to characterize their lasers. It will be shown that there is a minimum power necessary to reliably extract noise measurements. Later in this chapter, in section 3.6, the performance of the interferometer is demonstrated for different optical powers. The minimum power is found to be $P_{\text{min}} = 0.3\,\text{mW}$ at a wavelength of 780 nm.

3.3.1 Preparing the setup

In order to set up a new noise measurement, one needs to follow these steps in order to install the general setup for a laser.

The light is coupled into a polarization maintaining fiber with an efficiency high enough to reach at least P_{min} from section 3.6.

It is verified that the polarization of the incoupled light is matched to the polarization axis of the input fiber. This can be done by observing the beam power out of the fiber and behind a polarizer. Polarization drifts are then translated into power fluctuations. Check for polarization drifts by heating the fiber (holding the fiber with one hand is enough) and observing the power at the output of the fiber. If the power changes visibly, a half wave plate can be used before the fiber in-coupler to adjust the polarization at the input.

The fiber is inserted into the fiber out-coupler within the setup through the hole in the box and it is checked if the light makes it into the setup.

The photodetector is switched on and a T-piece is connected to the balanced channel (middle of three outputs).

Lastly, One of the cables from the photodetector is connected to the oscilloscope using 50 Ω termination.

For the tuning of the setup the following steps need to be followed:

Short arm

Fist, the light going through the long arm is blocked.

Next, one of the photodetector inputs is blocked. The two mirrors in the short arm and the mirror directly in front of the photodetector are adjusted to make sure the beam hits the other, uncovered photodetector input by observing the diode signal on the oscilloscope.

The input to the photodetector is unblocked and the other one is blocked. The mirror directly in front of the unblocked photodetector input is adjusted to make sure this input also receives light.

The signal of the two inputs should now be approximately the same. If this is not the case, one of the corresponding beams is not aligned ideally.

Long arm

The fiber coupling is adjusted using the mirror in front of the fiber in-coupler and the in-coupler itself to obtain sufficient light at the out-coupler. An efficiency of 80% is needed if the input power is equal to P_{min}. If more power is available the efficiency does not need to be as high. The power balance between the long and the short arm can be adjusted by turning the HWP after the input to the setup.

Again, it is checked if polarization drifts are relevant at the output of long fiber. If they are, the HWP in front of the in coupler to the long fiber is adjusted to minimize polarization drifts.

Next, one of the inputs of the photodetector is blocked. The piezo mirror and the fiber out-coupler of the long fiber are used to align the beam to be well overlapped with the beam of the short arm. If the beams are overlapped an interference signal should be visible.

The HWP after the input fiber out-coupler and the HWP after the piezo are adjusted to maximize the amplitude of the interference signal. By eye, it is observed if the spots are the same size at the photodetector input. If not, the position of the lens at the fiber out-coupler of the long fiber is adjusted.

The interference is futher maximized by beam walking in the short arm and fine-tuning the spot size. Ideally, a contrast of 80% is reached.

If the photodetector saturates or the shape does not show a clean cosine anymore, the input power into the setup is reduced (OD filters work well for this). The final maximum voltage should not exceed 1 V.

The second input is unblocked. The interference signal should now be centered around 0 V. If the amplitude drifts a lot, the polarization adjustment before the long fiber is redone.

3.3.2 Calibration measurement

The setup for the calibration measurement can be seen in figure 3.8(a). For the calibration measurement a high resolution oscilloscope is not needed.

In order to perform a calibration measurement one needs to follow these steps:

With a T-piece the output of the function generator is connected to the piezo and the oscilloscope.

A function generator is used to apply a ramp signal with 20 V Peak-to-Peak or higher (ranging from −10 V to +10 V) with a frequency of around 20 Hz to the piezo.

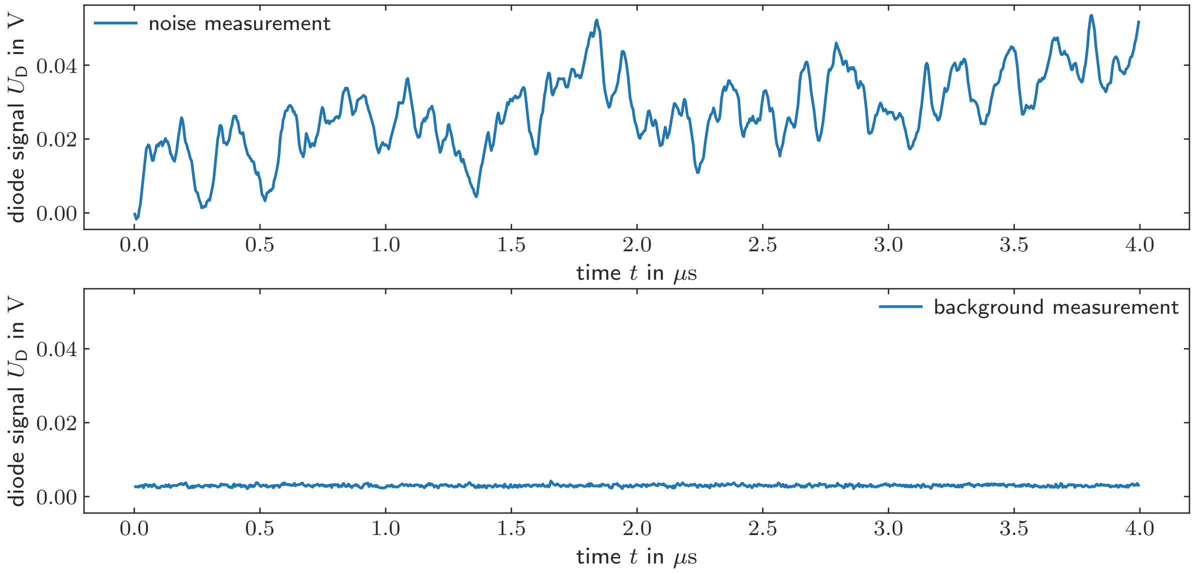

Figure 3.9: Small cut out of measured trace for measurement of noise (top) and background (bottom) measurement using a HR oscilloscope. Comparing the two measurements it is clear that the fluctuations in the background signal are much smaller than the fluctuations of the measured interference signal.

The trace of the ramp signal and the diode signal is saved as seen in figure 3.4.

A fit is performed to the resulting photodetector interference signal. This later allows the conversion of changes of the diode signal into relative phase differences between the beams of the two arms in the interferometer.

3.3.3 Noise Measurement

For the next two measurements the cabeling of the setup needs to be adjusted slightly as seen in figure 3.8(b). The function generator is disconnected from the piezo. Instead the slow output of the PID controller is connected as input to the piezo. One output of the balanced photodetector is plugged into the input of the PID-controller. This completes a feedback loop enabling to lock the piezo mirror at given phase difference between the two beams. The other output from the photodetector is plugged into either an oscilloscope with a high resolution (HR) or a spectrum analyzer. The PID-controller needs to be tuned by adjusting the input attenuation and the error offset in order to lock the signal close to 0 V.

For the following measurements a Teledyne LeCroy WavePro HD was used as a HR oscilloscope. Here a resolution of 100 million datapoints per second was used. To cover a frequency range of up to 50 MHz a resolution of at least 100 million points per second is needed. This equals a spacing of 10 ns between two adjacent datapoints.

The signal should be clearly visible and cover almost the entire screen in the vertical direction before saving. A small cut out part of the trace can be seen in 3.9. A large amount of datapoints should be recorded as this improves the resolution of the final noise spectrum. In the following measurements the traces usually contained 100 million datapoints. The power spectrum is obtained by calculating the Fourier transform of the trace. In order to handle the large amounts of data Welch's Method is used. This is discussed in more detail in section 3.4. The power spectrum can be converted to a noise spectral density $S_{\nu;i}$ using equation (2.19).

If a spectrum analyzer is used, it directly calculates the power spectral densities $S_{U;i}$. These can directly be converted to the noise spectral densities $S_{\nu;i}$ via equation (2.19).

3.3.4 Background Measurement

The background measurement is performed by blocking the short arm of the setup with a beam block. This e.g. allows the measurement of noise caused by polarization drifts and the noise of the electronics. A small part of the background trace can be seen in 3.9. The background spectrum is subtracted from the main spectrum.

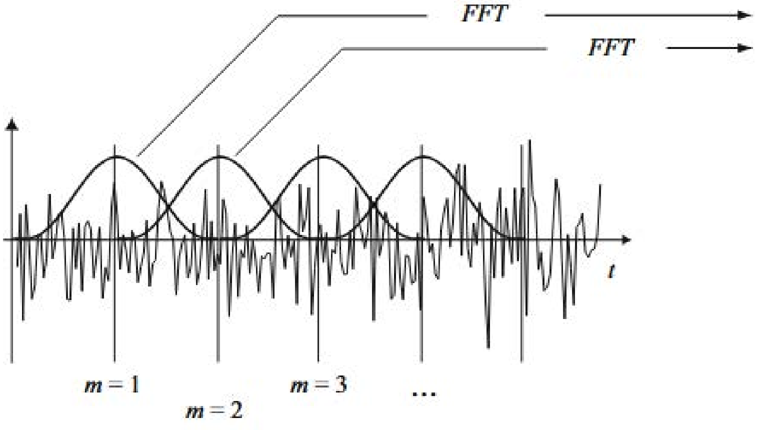

Figure 3.10: Schematic illustration of Welch's method for spectrum calculation. The data is seperated into overlapping segments of equal size, each of which is windowed and transformed via FFT. Source: [28]

3.4 Calculation of spectrum

To convert a signal measured with the HR oscilloscope, as the one shown in figure 3.9, to a power spectrum in frequency space we use a Fourier transform. We used Welch's method [26] imported from the Python Scipy module for the calculation of the spectrum. Welch's method is illustrated in figure 3.10. With Welch's method a signal is separated into segments of equal time spans. These segments have an overlap of 50% and each segment is multiplied by a Hann window of the following form [27]

$$w(n) = 0.5 \cdot \left(1 - \cos\left(\frac{2\pi n}{N}\right)\right) \tag{3.6}$$

where N is the length of each segment and $n = 0, 1, \ldots, N - 1$ corresponds to the samples in each segment. The application of a window function ensures that each segment is equal to zero at its edges to prevent spectral leakage. The overlap of the segments ensures that we do not lose too much information at the edges of each segment.

After multiplication with the window function each segment is then transformed using the Fast-Fourier-Transform algorithm (FFT). The calculated spectra are averaged over all the segments to obtain the final spectrum.

It is apparent in figure 3.11 and equation (3.6) that the choice of segment size for Welch's method is an important parameter. The size of the segments determines the maximum spectral resolution that can be extracted from the data as well as how many segments contribute to each point in the averaged spectrum. Increasing the segment size leads to a higher spectral resolution at the cost of averaging over less segments, i.e. losing accuracy in the spectrum. Smaller segment sizes allow better elimination of noise in the spectrum due to a higher number of averages. One must find a segment size that is sufficiently large to capture smaller trends in the spectrum with a sufficient spectral resolution and at the same time small enough to ensure that each point in the final spectrum is averaged over enough segments for a significant reduction of noise.

Finding an appropriate segment size is made further difficult by the logarithmic scaling of the frequency

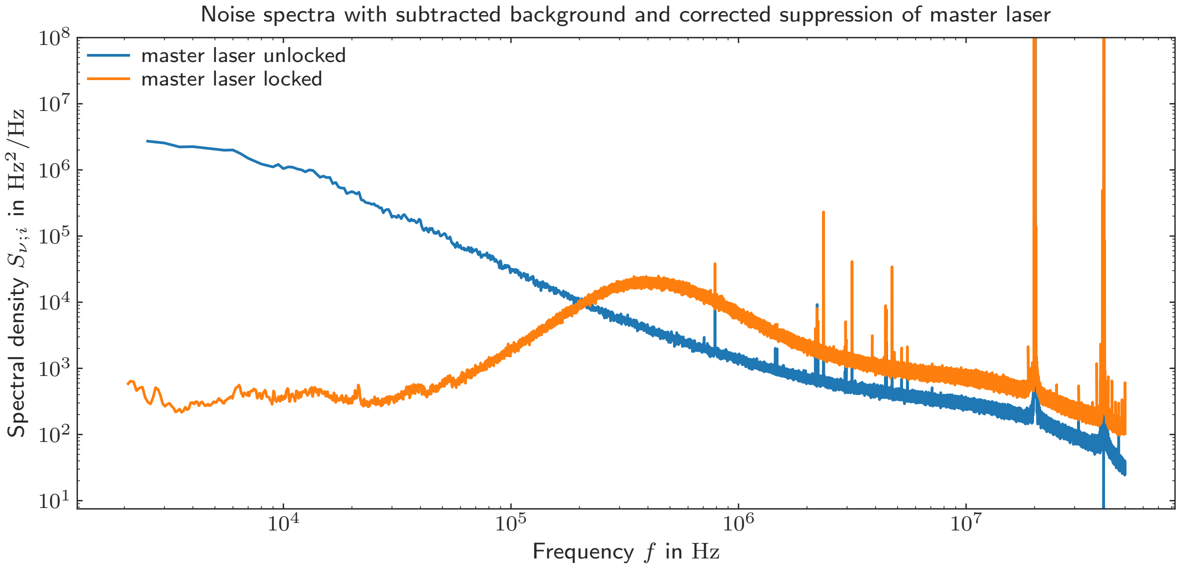

Figure 3.11: Frequency noise spectrum of ECDL (master laser) using Welch's method with a fixed segment length over the entire trace. It should be noted that data shown here have been corrected for suppression effects that will only be discussed in section 3.5

in the final spectrum. At lower frequencies the spacing between two adjacent frequencies appears much larger than for higher frequencies. Thus, for the low frequency range a higher frequency resolution is desired. At higher frequencies there are a lot more frequency components that are clustered together. This can be seen in figure 3.11. For high frequencies the spectral resolution does not need to be as high and it is desired to reduce the segment length in order to obtain a higher degree of averaging and therefore a cleaner spectrum.

There are different ways of extracting a power spectrum with high frequency resolution in the low-frequency range and a high degree of averaging in the high-frequency range.

3.4.1 LPSD method

The method named Logarithmic frequency axis Power Spectral Density (LPSD) presented by Troebs et. al. [29] calculates each Fourier frequency component individually with a Fourier-frequency dependent segment length. The segment length is adjusted for each frequency component such that the spacing between two frequencies is linear for a logarithmic axis. Therefore, in the final spectrum the points are equally spaced across the entire Fourier-frequency range. The parameters of the method allow a desired amount of Fourier-frequency components, a desired averaging amount given by the amount of segments, and a minimum averaging amount that ensures a certain degree of averaging remains across the entire spectrum.

The LPSD method shows promising results for small traces, but the routine is relatively demanding in terms of calculations and requires very long runtimes to process the large traces that are captured with the interferometer. Therefore, we implement an alternative.

3.4.2 Decade-wise Welch's method

In order to combine the high frequency resolution at low frequencies and high averaging degree at high frequencies from the LPSD method with the short runtime of the basic Welch's method, we implement a method that calculates the spectrum for each frequency decade separately with a decade-dependent segment length.

This idea was implemented by calculating the spectrum using Welch's method for each decade individually. The spectrum is usually calculated in the frequency range of 1 kHz up to below 50 MHz. The lower limit is determined by the length of the measured data trace and by the feedback loop which introduces some suppression of noise in the range between 0 Hz and 1 kHz. Therefore, 5 spectra are calculated in their respective decade and joined together. The amount of segments K_0 for the first decade was usually set to $1/50$ times the total length of the trace. The segment size then decays exponentially by the following formula

$$L(f) = \frac{N}{K_0 \cdot a^{\lfloor \log_{10}(f) \rfloor - \lfloor \log_{10}(f_{\text{min}}) \rfloor}} \tag{3.7}$$

a determines the growth of the amounts of segments. In the following spectra a was set to three so that the amount of segments is tripled for each decade.

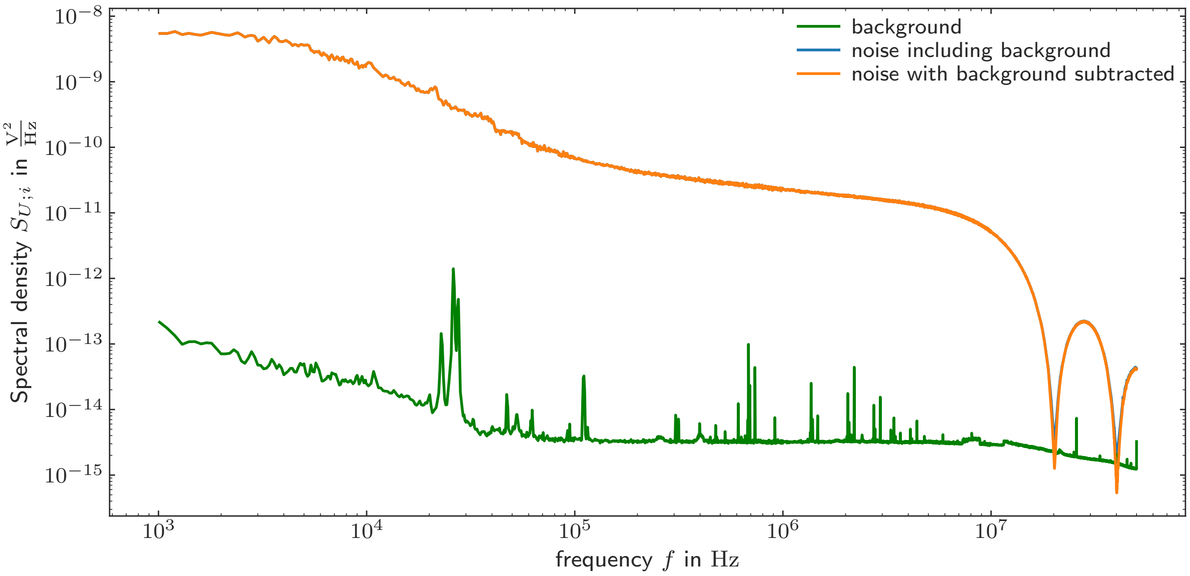

Figure 3.12: Uncorrected power spectral densities. The background is shown in green, the measured spectrum is shown in blue and the power spectral densities with a subtracted background are seen in orange.

3.5 Suppression correction

As discussed in section 2.4 and 2.5 the interferometer sensitivity is frequency dependent. For specific frequencies, destructive interference between noise components leads to a suppression of noise. This suppresion frequency is determined by the delay τ introduced by the arm length difference in the interferometer, and therefore by the length of the delay fiber.

Figure 3.12 shows the uncorrected power spectral an interference filter laser running at the wavelength of 780 nm. Fitting equation (2.25) to the spectrum of figure 3.12 allows precise estimation of τ, which is used in the conversion to the noise spectral densities $S_{\nu;i} = \frac{1}{s(f_i)} \cdot S_{U;i}$.

As seen in figure 3.11 there are points where the predicted sensitivity drops to basically zero, but where the measured spectrum maintains some finite value. when doing the correction for the suppression these very low values of the sensitivity are turned into peaks of the noise spectral densities at the suppression frequencies. These peaks are visible in figure 3.11.

Looking at the sensitivity $s_0 = 4\pi^2\tau^2 \left(\frac{dU_{\mathrm{Diode}}}{d(\Delta\varphi)} \Big|_{\Delta\varphi=\varphi_{\mathrm{lock}}} \right)^2$ (2.21) it can be seen that we essentially only have two degrees of freedom for varying the sensitivity. The first degree of freedom is the delay time τ. However, if τ is increased by for example reducing the length of the delay fiber within the setup, the suppression dips and therefore a decrease in sensitivity as seen in 2.3 appear at lower frequencies. This is due to the function shown going to zero for $f = m\frac{1}{\tau}$ where $m = 1, 2, 3, \ldots$. For our setup the first dip arises at a frequency of 2 MHz in good agreement with the delay of 49 ns caused by the 10 m delay fiber. If the delay is reduced, the suppression correction becomes relevant for a bigger part of the power spectrum and therefore adds an uncertainty to the final noise spectrum.

The second degree of freedom is given by adjusting the slope $\frac{dU_{\mathrm{Diode}}}{d(\Delta\varphi)} \Big|_{\Delta\varphi=\varphi_{\mathrm{lock}}}$ of the calibration measurement. It can be increased by feeding more power into the setup and by increasing the contrast

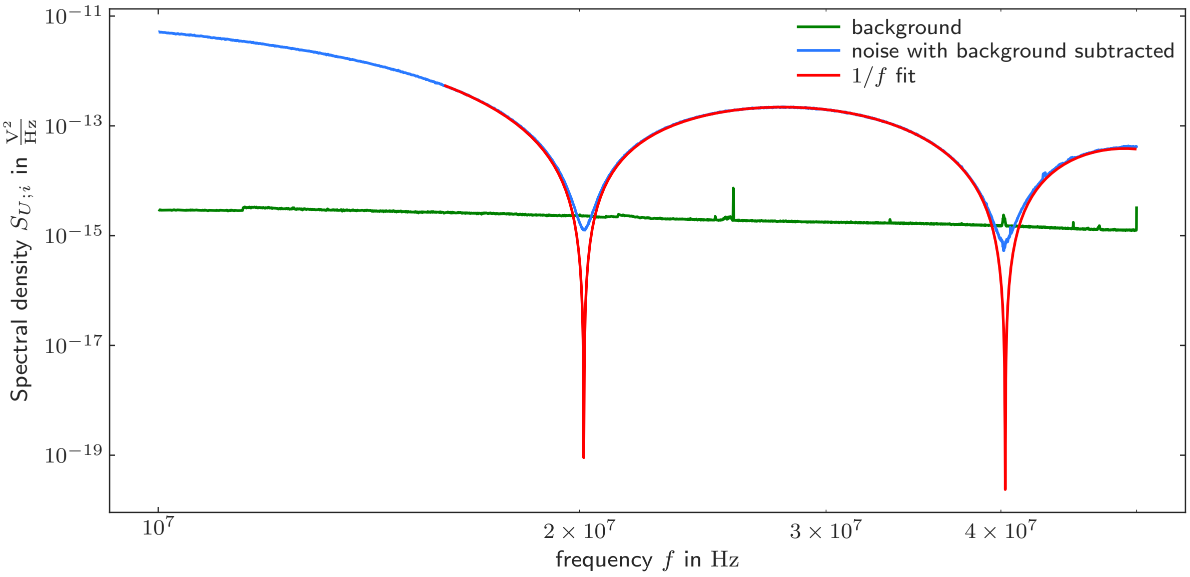

Figure 3.13: Uncorrected power spectrum with subtracted background (blue) with suppression fit for high Fourier-frequencies (red) and background shown in green.

$\frac{U_{\text{max}}-U_{\text{min}}}{U_{\text{max}}+U_{\text{min}}}$. We managed to get a contrast of up to 85% for our setup.

As can be seen in figure 3.11, the suppression correction leads to spikes in the spectrum due to the value of τ not being exact. To remove these spikes, the spectrum is cut out for all frequencies where the $1/f$ fit function is lower than the background itself as seen in 3.13. Depending on the quality of the suppression fit, this is not sufficient for all spectra. Therefore, a tunable larger percentage of the spectrum is cut out as well.

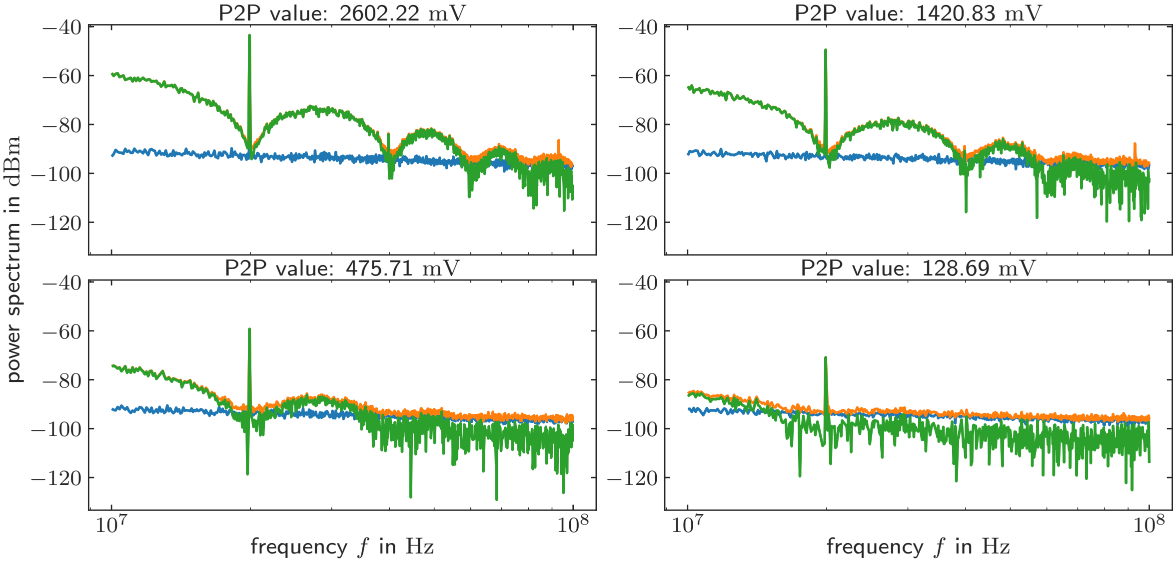

Figure 3.14: Measurements of the power spectrum of DLpro3 laser with varying P2P values of the calibration measurement; the blue curve is the measured background, the orange curve is the spectrum including the background and the green curve is the spectrum with the background subtracted

3.6 Ideal input power

The slope $\left.\frac{dU_{\text{Diode}}}{d(\Delta\varphi)}\right|_{\Delta\varphi=\varphi_{\text{lock}}}$ that determines the sensitivity can be varied with contrast, but also by increasing the intensity at the photo detector. In order to examine the influence of the input power on the quality of the measurement we performed a row of measurements with varying input powers. This was done by placing different OD Filters in the path of the light right after the fiber coupler into the setup. The following measurements were done using the spectrum analyzer looking at the power spectrum measured in dBm.

The spectrum in the higher frequency range becomes a lot cleaner for higher Peak-to-Peak values (P2P) of the calibration measurement. Since the P2P value grows with input power the quality of the measurements improves with increasing input power. The relationship between the P2P value of the calibration and the input power will be discussed later. For now a minimum P2P value will be determined to ensure a successful and clean measurement.

As seen in 3.14 the suppression dips at frequencies higher than 30 MHz are not clearly distinguishable anymore for measurements with P2P values lower than 475 mV. As seen in 3.15 the dips become slightly visible at P2P values of around 1 V. Since usually the final noise spectrum is only calculated up to frequencies of less than 50 MHz the minimum P2P value for a successful measurement was set to

$$U_{\text{P2P; min}} = 1\,\text{V} \tag{3.8}$$

The photodetector has a maximum output voltage of ±1 V for linear operation [30]. Therefore, the maximal P2P value was set to

$$U_{\text{P2P; max}} = 2\,\text{V} \tag{3.9}$$

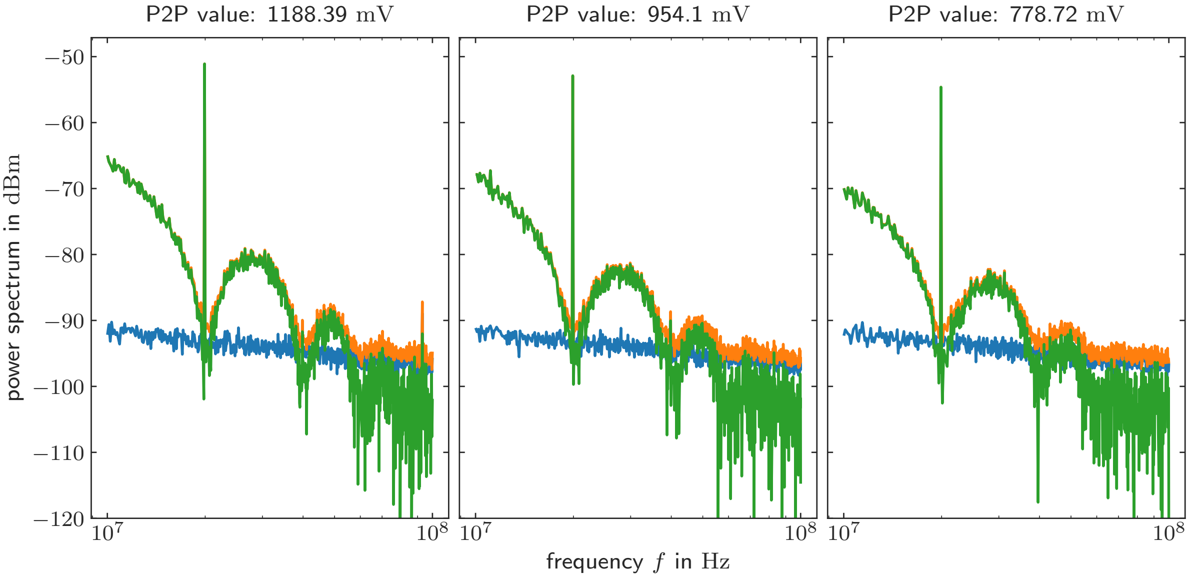

Figure 3.15: Measurements of the power spectrum of DLpro3 laser with varying P2P values of the calibration measurement in a smaller range; the blue curve is the measured background, the orange curve is the spectrum including the background and the green curve is the spectrum with the background subtracted

For the conversion of a P2P value to the power P_{in} at the input of the setup after the fiber in-coupler we measured the P2P value for different input powers. This can be seen in 3.17. A linear relationship can clearly be seen.
The fit function has the following form

$$U_{\text{P2P; 780}}(P) = (3.35 \pm 0.06)\ \frac{\text{V}}{\text{mW}} \cdot P + (-0.02 \pm 0.02)\ \text{mV} \tag{3.10}$$

Therefore the minimum Power corresponding to $U_{\text{P2P; min}} = 1\ \text{V}$ is approximately

$$P_{\text{min}} = 0.3\ \text{mW} \tag{3.11}$$

and

$$P_{\text{max}} = 0.6\ \text{mW} \tag{3.12}$$

3.6.1 Larger wavelengths

The values of P_{min} and P_{max} given in equation (3.11) and (3.12) are determined for a laser at 780 nm. However, the interferometer can be used for characterizing laser noise for a span of wavelengths. The setup is build with b-coated optics, meaning that all passive components except for the HWPs can be used for the wavelength range of 650 nm to 1050 nm. If the setup is used for a different wavelength as will be the case later in this thesis, the values of P_{min} and P_{max} must be adjusted according to the sensitivity of the photo detector. The photo detector sensitivity peaks at 780 nm. For longer wavelengths the sensitivity decreases as seen in figure 3.16.

For higher wavelengths the sensitivity of the photodetector decreases as seen in 3.16. This means that

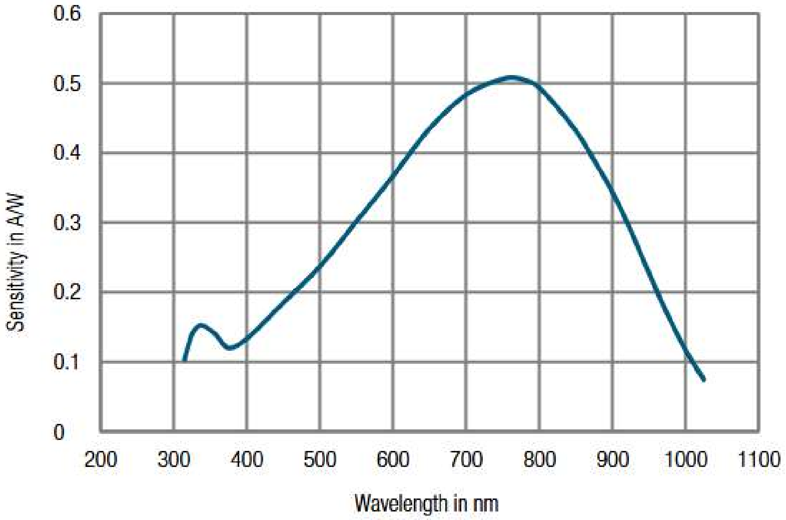

Figure 3.16: Sensitivity of balanced photodetector used in this setup [30]. The peak of the sensitivity is at 780 nm and falls off for higher wavelengths.

more input power is needed when performing measurements of lasers running at higher wavelengths.

We have performed measurements of two lasers running at 960 nm and 1012 nm and measured the P2P value-input power relationship. The contrast was again at around 80% but the fiber coupling within the setup was only at 50%. Therefore, the input power needs to be corrected in order to simulate the case of a fiber coupling of 80%, which is easily achievable for most measurements.

The Intensity $I(r)$ that is measured at the photodetector divided by the input Intensity I_0 when taking losses at the fiber coupling in the long arm into account is given by

$$\frac{I(r)}{I_0} = \frac{r}{2-r} \tag{3.13}$$

Where $0 \leq r \leq 1$ is the fiber coupling efficiency within the setup. Therefore, at an efficiency of $r = 80\%$ the power falls off to 67% of the input power. At an efficiency of $r = 80\%$ the power falls off to 33% of the input power.

Therefore, the minimal power needs to be corrected by the factor of

$$\alpha = \frac{I(0.8)}{I(0.5)} = \frac{I_0/I(0.5)}{I_0/I(0.8)} = 0.5 \tag{3.14}$$

to calculate the necessary minimal input power in the case of a fiber coupling of 80%. Again, a linear relationship can be seen in 3.17 (excluding the largest datapoint for the 960 nm measurement).

The fit functions for the two measurements are the following:

$$U_{\mathrm{P2P;\,960}}(P) = (0.99 \pm 0.01)\ \frac{\mathrm{V}}{\mathrm{mW}} \cdot P + (-0.005 \pm 0.001)\ \mathrm{V} \tag{3.15}$$

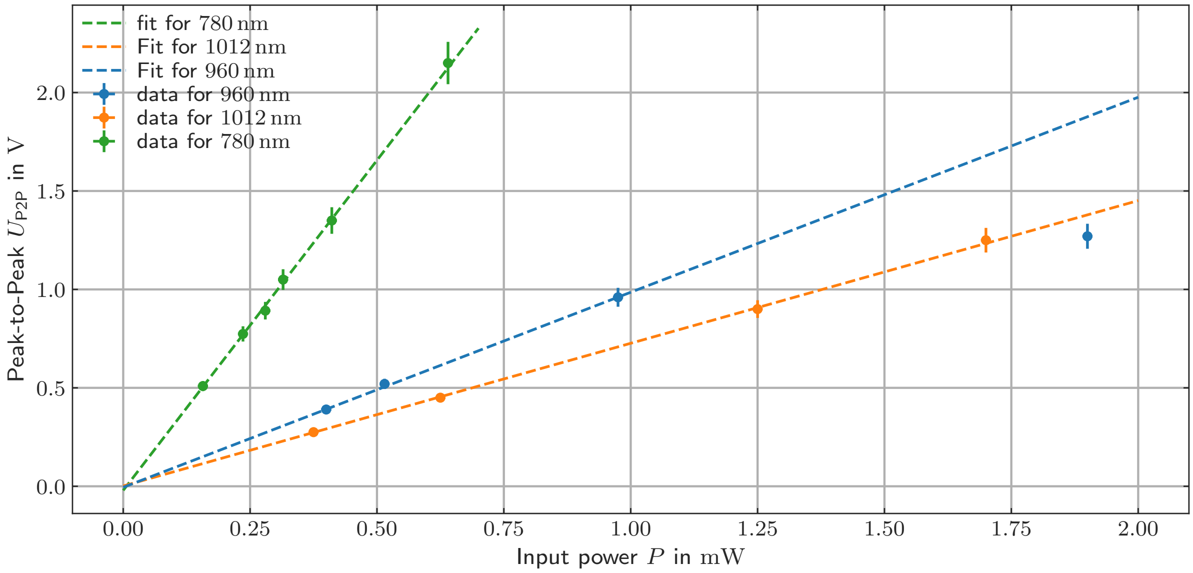

Figure 3.17: Conversion of input power to P2P value for 3 lasers at different wavelengths. The dashed lines are the linear fits to the measured data. The measurements were performed with a contrast of 80% and (corrected to) a fiber coupling efficiency of 80% within the setup.

$$U_{\mathrm{P2P;\,1012}}(P) = (0.72 \pm 0.01)\ \frac{\mathrm{V}}{\mathrm{mW}} \cdot P + (0.002 \pm 0.006)\ \mathrm{V} \tag{3.16}$$

As can be seen in 3.17, the slope of each of the curves is related to the sensitivity of the photodetector. This is in accordance with the change of the sensitivity depicted in 3.16.

All the corresponding minimal P2P values and Powers are shown in table 3.1 (including the fiber coupling correction).

With the measurement protocol and the optimal power ranges for the different wavelengths established we can now move on to the characterization of laser noise.

	780 nm	960 nm	1012 nm
P_{min} in mW	0.3	1	1.4
P_{max} in mW	0.6	2	2.75
$U_{\mathrm{P2P;\,min}}$ in V	1	1	1
$P_{\mathrm{P2P;\,max}}$ in V	2	2	2

Table 3.1: Minimal and maximal input Powers and P2P values for different wavelengths at a contrast of 80% and fiber coupling efficiency within the setup of 80%

CHAPTER 4

Noise spectral density for various laser types

In the following, the frequency noise measurements of various lasers are shown and discussed. Most of the lasers were measured at a wavelength of 780 nm, but measurements at 960 nm and 1012 nm were also conducted. One of the lasers is a distributed feedback laser with an integrated cavity. All other lasers are external-cavity diode lasers with either a grating or an interference filter as a wavelength discriminator. Two include a built-in tapered amplifier that greatly increases the output power.

In our experiments, we are using one grating laser at 780 nm as one part of the two-photon Rydberg excitations. The second laser couples the intermediate state 5P3/2 to Rydberg states nS1/2 with a wavelength of 480 nm. This wavelength is generated with a second harmonic generation crystal from a fundamental wavelength at 960 nm. As the interferometer built in the course of this thesis is designed for the near-infrared range, we only measure the noise spectral densities of the fundamental wavelength of 960 nm.

Our portable setup has the advantage that it can be placed anywhere in the lab and proved to be stable enough to acquire noise spectra fast and reproducibly. Furthermore, the setup allows to measure the noise spectral density of any propagating laser beam and does not rely on an in-loop signal as e.g. from a control loop error signal. Thereby, we measure here the noise spectral densities for lasers as they are sent onto the experimental vacuum chamber.

We expect the curve to have the shape of $1/f$ noise. With double logarithmic scaling this has the form of a linear negative slope. This shape is only approximately met.

4.1 External-cavity diode laser

The external-cavity diode laser (ECDL) from Toptica is a tunable grating laser which is run at the wavelength of 780 nm [31]. It has an output power of 100 mW. These ECDLs are the lasers that are most used in our labs. One of these provides the few-photon 780 nm pulses that are used in the Rydberg experiments.

A diode laser is a semiconductor laser based on laser diodes. They consist of a highly doped p-n junction or a p-i-n junction. When a forward electrical bias is applied, holes and electrons are moved into the depletion region where they recombine and generate photons. The energy of the photons is determined by the gap energy.

In an ECDL the laser diode is usually placed into a larger laser cavity as seen in 4.1(a). The diode has an anti-reflection coating on the right-hand side that allows the photons to be emitted onto the grating

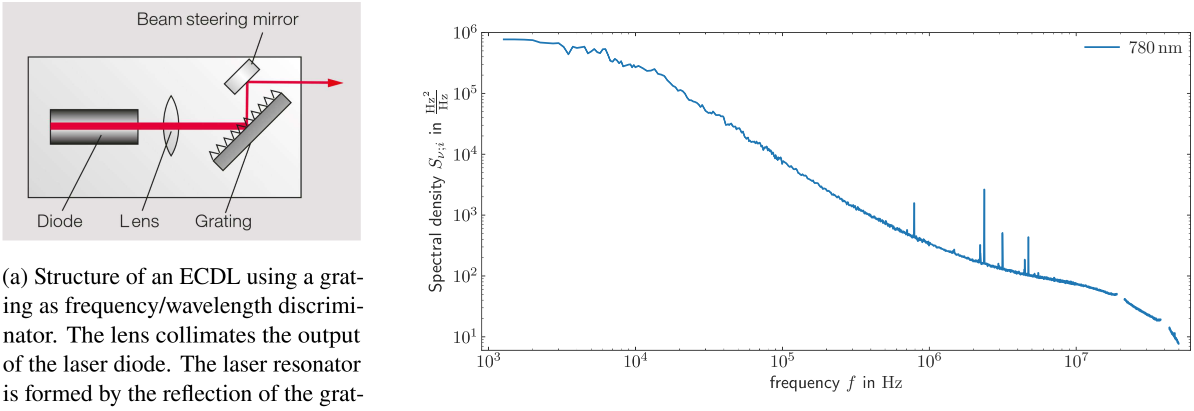

(a) Structure of an ECDL using a grating as frequency/wavelength discriminator. The lens collimates the output of the laser diode. The laser resonator is formed by the reflection of the grating and the back side of the laser diode. The beam steering mirror can be used to control the beam pointing, if the grating is rotated. [33]

(b) Noise spectral density for an ECDL operating at 780 nm. The spectrum is measured with the setup discussed in Chapter 3 and the suppression dips are compensated for.

Figure 4.1: Structure and noise spectral density of an unlocked ECDL operating at a wavelength of 780 nm with a grating used as a wavelength discriminator

via a lens. The grating allows the tuning of the wavelength and partially reflects the tuned light back into the diode, forming a resonator [32].

Its noise spectral density can be seen in 4.1(b). In the experiments, the noise spectral density around 1 MHz is the most relevant and influences the coherent excitation between the ground and Rydberg state [25]

4.2 External-cavity diode lasers including a tapered amplifier

The TA pro from Toptica is a Tapered Amplifier Laser System, and we have a system that operates at a wavelength of 1012 nm. It follows the same principle as an ECDL but includes a Tapered Amplifier (TA) that strongly amplifies the output power. It can reach powers of up to 4 W [34].

A Tapered Amplifier is an optical amplifier where the cross-section of the beam is gradually increased within a gain medium as seen in 4.2(a). After exiting the amplifier the width of the beam is again reduced with a focusing lens.

The second ECDL including a TA we measured is the TA-SHG pro laser by Toptica which also includes a Second-Harmonic-Generation (SHG) crystal that allows frequency doubling into the 480 nm range at the output [35]. We only measured the noise of this laser by extracting light from a side-arm before the SHG crystal. The light from the side output of the laser has a wavelength of 960 nm. We did not measure the light at 480 nm as this would require the exchange of all optical elements and not just the wave-plates. The anti-reflection coatings in the current setup are chosen for the near infrared range.

The two noise spectral densities are shown in 4.2(b).

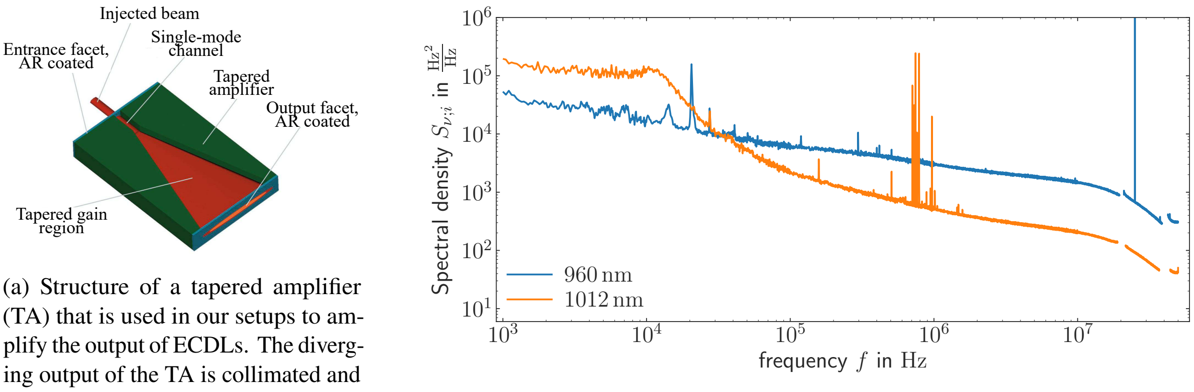

(a) Structure of a tapered amplifier (TA) that is used in our setups to amplify the output of ECDLs. The diverging output of the TA is collimated and adjusted in size in the experimental setup by a set of lenses. The sketch is adapted from [36]

(b) Noise spectral densities of ECDLs that are amplified with tapered amplifieres respectively. The two traces are recorded for different setups operating at wavelength of 960 nm and 1012 nm.

Figure 4.2: Structure of a TA and noise spectral densities of unlocked ECDLs including a TA for two different wavelengths

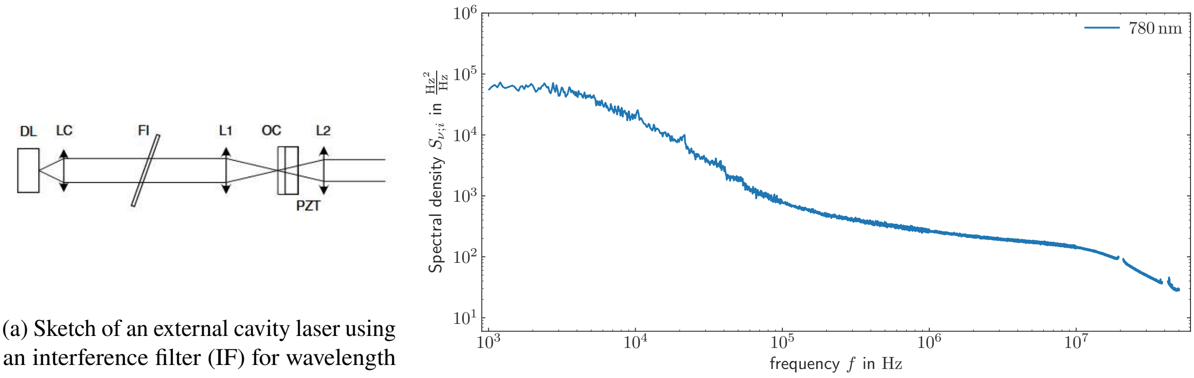

(a) Sketch of an external cavity laser using an interference filter (IF) for wavelength selection adapted from [37]

(b) Noise spectral density of IFL

Figure 4.3: Structure of an IFL; DL: laser diode; LC: collimating lens; OC: partially reflective out-coupler; PZT: piezo-electric transducer actuating OC; L1, L2: lenses. The noise spectral density of the unlocked IFL operating at a wavelength of 780 nm is shown in 4.3(b)

4.3 Interference filter laser

The measured laser is a home-built external-cavity Interference Filter diode laser (IFL). The laser is built upon external-cavity interference-filter-stabilized diode lasers developed at SYRTE labratories [37]. The setup can be seen in 4.3(a). The light emitted from the laser diode is reflected back into the diode using a cats eye consisting of the lens L1 and outcoupling mirror (OC). The wavelength discriminator is given by the IF which is used as a bandpass filter and can be tuned by tilting the filter. In principle this configuration allows for very narrow linewidths and reduced frequency noise.

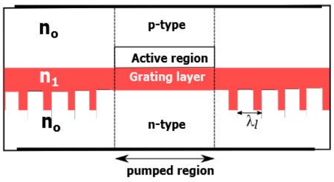

(a) Schematic of longitudinal sections in a DFB diode. A periodic modulation of the refractive index is created by the differing refractive indices n_1 and n_o on either side of the grating. The grating period is denoted by λ_l. Source: [39]

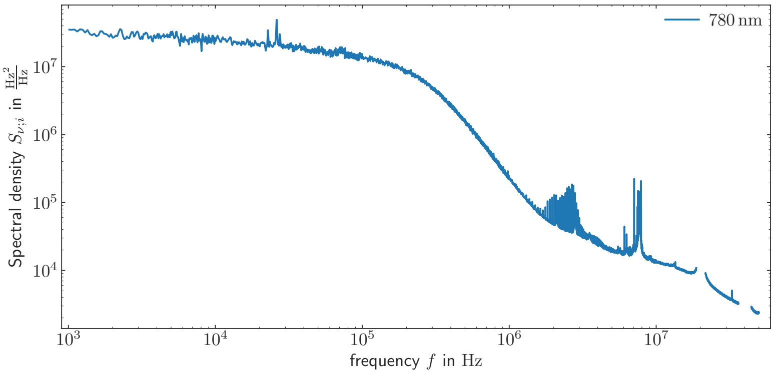

(b) Noise spectral density of DFB laser operating at a wavelength of 780 nm

Figure 4.4: Structure and noise spectral density of a distributed feedback laser

4.4 Distributed feedback laser

The Balalaika Laser is a home-built Distributed Feedback (DFB) Laser running at the wavelength of 780 nm. As opposed to an ECDL the grating is integrated into the diode as shown in 4.4(a). While this makes the fabrication a lot easier, there is a trade off by an increased linewidth and therefore high frequency noise.

Measurements of photon-number dependent phase shifts however show that the DFB is less noisy for frequencies below 1 kHz compared to an ECDL [38]. This is due to the integrated structure of the grating which makes the laser less susceptible to mechanical vibrations as a noise source. This reduction in noise is not seen in the frequency range we measured as it is below the kHz region. Therefore, as can be seen in 4.4(b), the DFB laser exhibits very high noise levels in the measured range compared to the ECDLs and IFL we measured.

4.5 Comparison of all measured lasers

In Figure 4.5 a comparison of all free-running lasers that are mentioned above is shown.

The IFL shows very low levels of frequency noise. It is less noisy compared to the measured unlocked ECDLs in the region of 10 kHz to 1 MHz. Its curve flattens out for higher Fourier-frequencies.

The ECDL+TA at 960 nm shows the lowest noise levels for frequencies up to 10 kHz. It has a very flat curve that seems to be dominated by white noise. Therefore it shows very high noise levels in the MHz region compared to the other ECDLs. This could be a problem for experiments on the microsecond time scale.

The ECDL has the lowest noise levels at frequencies above 20 MHz where it drops to a spectral density of $S_\nu = 15\,\mathrm{Hz}^2/\mathrm{Hz}$. Its spectral density follows a very steep curve and therefore shows the highest levels of noise in the low frequency region compared to the other ECDLs. As the drop at the upper end of the spectrum occurs for all lasers, it can possibly be attributed to the drop of the sensitivity due to the suppression dips.

The noise of the ECDL+TA at 1012 nm is dominated by white noise for frequencies up to 10 kHz and falls off for higher frequencies similar to the IFL.

The noise of the ECDLs varies from each laser. They all exhibit noise in the region of $S_\nu = 100\,\mathrm{Hz}^2/\mathrm{Hz} - 10{,}000\,\mathrm{Hz}^2/\mathrm{Hz}$ for the largest part of the spectrum.

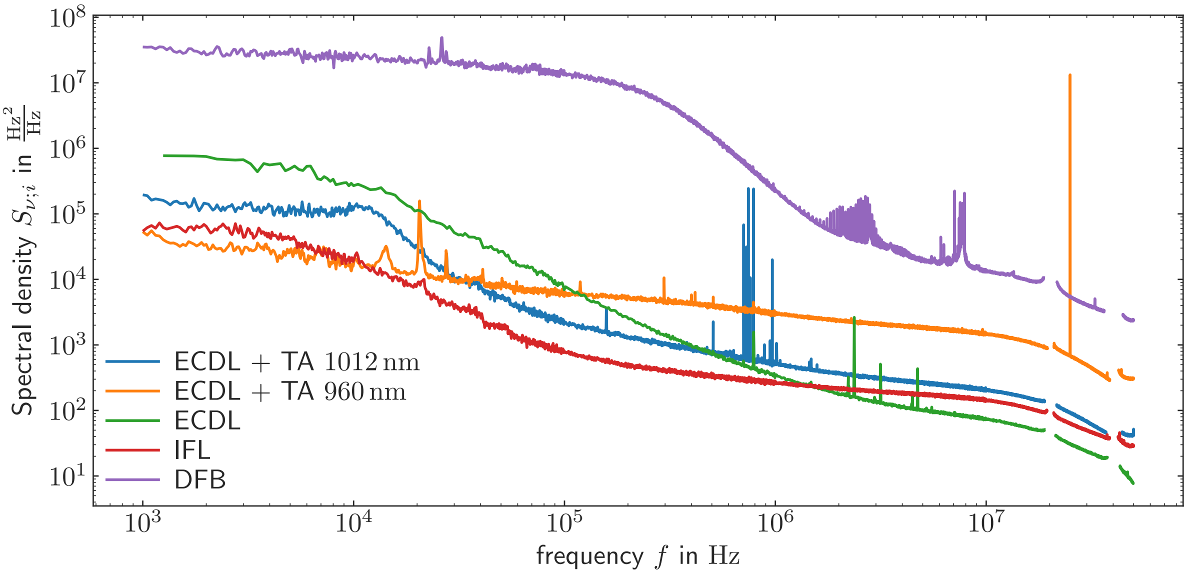

Figure 4.5: Noise spectra of all measured lasers

4.6 Frequency noise of locked lasers

In typical cold atom experiments, the lasers are stabilized in their frequency by feedback loops. We refer to the stabilized lasers as locked lasers.

The noise spectra are recorded outside of the frequency stabilization loop and allow an independent measure of the noise spectral characteristics of lasers used in our cold atom experiment.

The noise spectrum of the free-running ECDL is shown in 4.6 where the comparison between the locked and unlocked laser can be seen. The locked laser is significantly less noisy for frequencies below 200 kHz, which is the frequency range where the feedback loop acts. Its noise exceeds the noise of the unlocked laser for frequencies above 200 kHz. The laser exhibits large amounts of noise at 1 MHz and a peak can be seen, a so called servo-bump [40]. The servo bump is caused by the fact that the feedback loop has internal signal delays, which cause the feedback to be out of phase with the actual noise. This leads to the noise being amplified instead of compensating for it. Therefore, a total reduction of frequency noise across the entire spectrum is not possible.

The ECDL is used as a reference laser in order to stabilize other lasers used in the experiment.

The noise spectrum of the TA lasers can also be seen in 4.6 again comparing the locked to the unlocked laser. The same behavior of a reduction of noise in the low frequency region and creation of a servo bump at around 1 MHz can again be seen.

When comparing the three lasers, it can be seen that the degree of noise suppression in the 10 kHz region varies. The reduction of noise is highest for the 960 nm laser, followed by the 1012 nm and lowest for the ECDL. It can also be seen that the lasers with stronger noise suppression in the low frequency region exhibit larger servo bumps at higher frequencies.

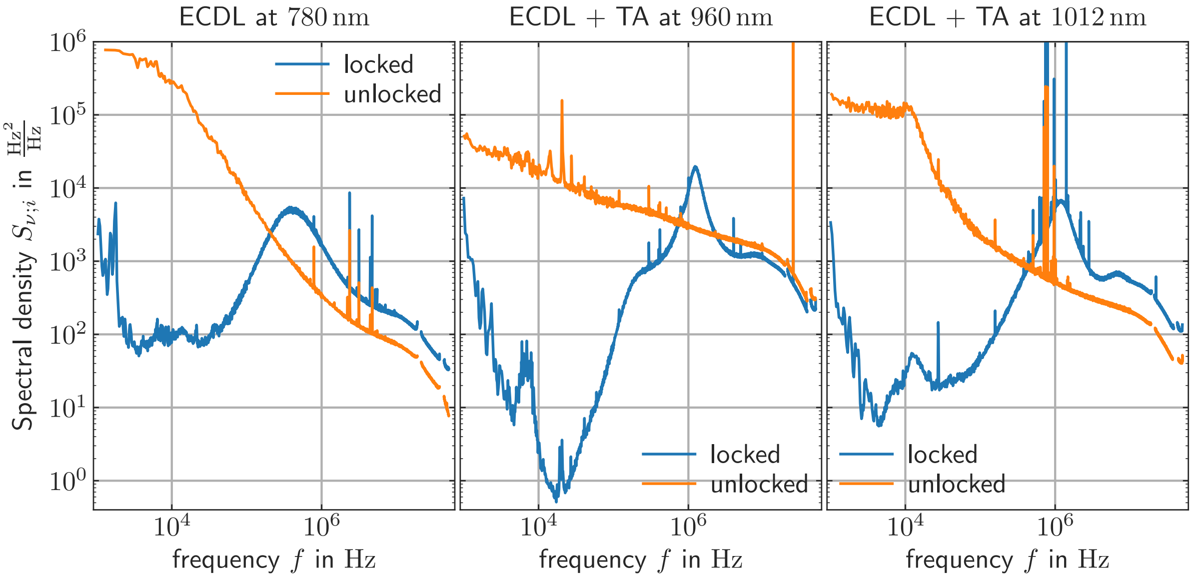

Figure 4.6: Noise spectral densities of 3 ECDLs running at different wavelengths. Each laser was measured while free-running (unlocked) and while being actively frequency stabilized (locked).

CHAPTER 5

Conclusion and outlook

In this thesis, a compact and portable system for characterizing laser frequency noise using a balanced Mach-Zehnder interferometer was developed and successfully applied. The setup allows precise measurement of frequency noise spectral densities for wavelengths ranging from 780 nm to 1012 nm. It can give crucial insights on the frequency noise of a laser used in experiments where decoherence plays a role when the laser is used for e.g. driving the transitions to Rydberg states.

A theoretical framework was presented, covering the origins of laser frequency noise and the impact of both quantum and technical noise sources. The derivation of the system's sensitivity and its frequency-dependent suppression effects was crucial for accurate interpretation of the measured spectra. Special attention was given to the behavior of the piezoelectric mirror actuator, including hysteresis and non-linearities, which were carefully characterized through calibration measurements.

The implementation of the setup involved a detailed alignment procedure, sensitivity optimization and systematic data acquisition using an oscilloscope or a spectrum analyzer. Welch's method was employed for spectral analysis, and additional correction methods were introduced to account for background noise and suppression effects. Measurements were successfully performed on a range of diode lasers, including ECDLs, interference filter lasers and lasers with tapered amplifiers, highlighting differences in their noise characteristics and the effect of active frequency stabilization.

The system proved to be versatile and robust, capable of resolving frequency noise features up to several tens of megahertz. With a minimum required input power of 0.3 mW (at 780 nm) and high contrast interference, the setup offers a reliable tool for laser diagnostics in laboratory environments.

Outlook

A possibility for further enhancing the sensitivity of the setup, that was not investigated so far, is to use the monitor outputs for the calibration measurement. The monitor outputs of the balanced photodetector have a higher maximum output voltage of 10 V compared to the balanced output with 1 V (for linear operation) [30]. Therefore, the output of the individual monitor outputs can be converted to an amplitude of the calibration measurement used so far. When performing the measurement, the balanced output is then used with a peak-to-peak value that would exceed the maximum output voltage of the balanced output. Since the interferometer for the noise spectrum measurements only operates in a small range around 0 V, the signal will stay linear and we obtain a much higher sensitivity due to the increased slope around 0 V.

One possible application is to use the interferometer setup in a feed-forward loop to actively compensate any detected frequency variations using an electro-optical modulator. This was performed with great success by Denecker et al. [8]. It avoids the limitations of frequency stabilization via a feedback loop, which is limited in the high frequency ranges due to signal delays in the loop. Therefore, it can greatly decrease laser noise.

Bibliography

[1] M. Malinauskas, A. Žukauskas, S. Hasegawa, Y. Hayasaki, V. Mizeikis, R. Buividas, and S. Juodkazis, *Ultrafast laser processing: From science to industry*, CIRP Annals **70** (2021) 717.

[2] N. Nickerson and ..., *Microscopic Characterization of Scalable Coherent Rydberg Superatoms*, Physical Review X **5** (2015) 031015.

[3] J. Kumlin, C. Braun, C. Tresp, N. Stiesdal, S. Hofferberth, and A. Paris-Mandoki, *Quantum Optics with Rydberg Superatoms*, arXiv:2312.03649 [quant-ph], Submitted on 6 Dec 2023, 2023.

[4] D. P. Ornelas-Huerta, A. N. Craddock, E. A. Goldschmidt, A. J. Hachtel, Y. Wang, P. Bienias, A. V. Gorshkov, S. L. Rolston, and J. V. Porto, *On-demand indistinguishable single photons from an efficient and pure source based on a Rydberg ensemble*, Optica **7** (2020) 813.

[5] D. Tiarks, S. Schmidt-Eberle, G. Rempe, and S. Dürr, *Optical pi Phase Shift Created with a Single-Photon Pulse*, Science Advances **2** (2016) e1600036.

[6] T. Stolz, H. Hegels, M. Winter, B. Röhr, Y.-F. Hsiao, L. Husel, G. Rempe, and S. Dürr, *Quantum-Logic Gate between Two Optical Photons with an Average Efficiency above 40%*, Physical Review X **12** (2022) 021035.

[7] Y. Jiao, C. Li, X.-F. Shi, J. Fan, J. Bai, S. Jia, J. Zhao, and C. S. Adams, *Suppression of Motional Dephasing Using State Mapping*, Physical Review Letters **134** (2025) 053604.

[8] T. Denecker, Y. T. Chew, O. Guillemant, G. Watanabe, T. Tomita, K. Ohmori, and S. de Léséleuc, *Measurement and feed-forward correction of the fast phase noise of lasers*, Phys. Rev. A **111** (2025) 042614.

[9] S. Schneider and G. J. Milburn, *Decoherence in ion traps due to laser intensity and phase fluctuations*, Physical Review A **57** (1998) 3748.

[10] S. de Léséleuc, D. Barredo, V. Lienhard, A. Browaeys, and T. Lahaye, *Analysis of imperfections in the coherent optical excitation of single atoms to Rydberg states*, Physical Review A **97** (2018) 053803.

[11] J. Bechhoefer, *Feedback for physicists: A tutorial essay on control*, Reviews of Modern Physics **77** (2005) 783.

[12] H. M. Wiseman, *Light amplification without stimulated emission: Beyond the standard quantum limit to the laser linewidth*, Phys. Rev. A **60** (1999) 4083.

[13] A. L. Schawlow and C. H. Townes, *Infrared and Optical Masers*, Phys. Rev. (1940).

[14] K. Numata, A. Kemery, and J. Camp,
Thermal-Noise Limit in the Frequency Stabilization of Lasers with Rigid Cavities,
Phys. Rev. Lett. **93** (2004) 250602.

[15] V. V. Vassiliev, D. S. Chuchelov, S. A. Zibrov, M. I. Vaskovskaya, E. A. Tsygankov, K. M. Sabakar, and V. L. Velichansky, *Direct Comparison of the Acoustic Stability of External Cavity Diode Lasers with Different Types of External Cavity*,
Bulletin of the Lebedev Physics Institute **50** (2023) 409.

[16] F. N. Hooge, "1/f Noise Sources," *1/f Noise*, ed. by J. Sikula and M. E. Levinshtein, vol. 168, NATO Science Series II: Mathematics, Physics and Chemistry, Springer, Dordrecht, 2004 3, ISBN: 978-1-4020-2169-5.

[17] D. Kim, M. Harfouche, H. Wang, C. T. Santis, Y. Vilenchik, N. Satyan, G. Rakuljic, and A. Yariv, *Consequences of quantum noise control for the relaxation resonance frequency and phase noise in heterogeneous Silicon/III–V lasers*,
Scientific Reports **12** (2022) 312, Published January 10, 2022.

[18] M. J. O'Mahony and I. D. Henning,
Semiconductor laser linewidth broadening due to 1/f carrier noise,
Electronics Letters **19** (1983) 1000.

[19] S. Schmidt-Eberle, *Phase and Frequency Locking of Diode Lasers*,
Application Note, TOPTICA Photonics AG, Published online April 13, 2021, 2021.

[20] E. D. Black, *An introduction to Pound–Drever–Hall laser frequency stabilization*,
Am. J. Phys. (2001).

[21] Physik Instrumente, *Fundamentals of Piezo Technology*, `https://www.pi-usa.us/en/expertise/technology/piezo-technology/fundamentals`, 2024.

[22] K. P. Zetie, S. F. Adams, and R. M. Tocknell, *How does a Mach–Zehnder interferometer work?*
Physics Education **35** (2000) 46.

[23] P. Cladé, *Oscillations de Bloch d'atomes ultrafroids et mesure de la constante de structure fine*,
PHD-Thesis: Université Pierre et Marie Curie - Paris, 2005.

[24] M. Metternich, *Laser Frequency Stabilization to Optical and Atomic References*,
Bachelor thesis: Universitaet Bonn, 2024.

[25] S. Schroers, *Impact of Laser Frequency Noise on Rydberg Superatom Dephasing*,
Master thesis: Universitaet Bonn, 2025.

[26] P. D. Welch, *The use of fast Fourier transform for the estimation of power spectra: A method based on time averaging over short, modified periodograms*,
IEEE Transactions on Audio and Electroacoustics **15** (1967) 70.

[27] S. G. Braun, "WINDOWS," *Encyclopedia of Vibration*,
ed. by S. G. Braun, D. J. Ewins, and S. S. Rao, Academic Press, 2001 1587.

[28] A. Brandt and S. Manzoni,
"Introduction to Spectral and Correlation Analysis: Basic Measurements and Methods,"
Handbook of Experimental Structural Dynamics, ed. by R. Allemang and P. Avitabile,
New York, NY: Springer New York, 2020 1, ISBN: 978-1-4939-6503-8.

[29] M. Tröbs and G. Heinzel,
Improved spectrum estimation from digitized time series on a logarithmic frequency axis,
Measurement **39** (2006) 120.

[30] FEMTO Messtechnik GmbH,
HBPR-500M-10K-SI-FST High-Speed Balanced Photoreceiver — Datasheet,
Version R3, Dokumentdatum 05.März.2024,
FEMTO Messtechnik GmbH, Berlin, Germany, 2024.

[31] TOPTICA Photonics AG, *DL pro Tunable External-Cavity Diode Laser*, `https://www.toptica.com/products/tunable-diode-lasers/ecdl-dfb-lasers/dl-pro`, 2025.

[32] C. Ye, *Tunable External Cavity Diode Lasers*, Singapore; Hackensack, NJ: World Scientific, 2004 xiii, 262, ISBN: 9812560882, 9789812560889.

[33] TOPTICA Photonics AG,
Tunable Diode Lasers: Turning Laser Diodes into Tunable Diode Lasers, `https://www.toptica.com/technology/technical-tutorials/tunable-diode-lasers`,
Accessed: 22 July 2025, 2025.

[34] TOPTICA Photonics AG, *TA pro - High-Power Tunable Diode Laser*, `https://www.toptica.com/products/tunable-diode-lasers/amplified-lasers/ta-pro`,
Accessed: 2025-07-11, TOPTICA Photonics AG, n.d.

[35] TOPTICA Photonics AG, *TA SHG pro - Frequency-Converted Tapered Amplifier Laser*,
`https://www.toptica.com/products/tunable-diode-lasers/frequency-converted-lasers/ta-shg-pro`, Accessed: 2025-07-11, TOPTICA Photonics AG.

[36] RP Photonics AG, *Tapered Amplifiers*,
`https://www.rp-photonics.com/tapered_amplifiers.html`, Accessed: 2025-07-11,
RP Photonics AG, n.d.

[37] X. Baillard, A. Gauguet, S. Bize, P. Lemonde, P. Laurent, A. Clairon, and P. Rosenbusch,
Interference-filter-stabilized external-cavity diode lasers,
Optics Communications **266** (2006) 609.

[38] A. C. Nitsch, *Interferometer setup for detecting photon-number dependent phase shifts*,
Bachelor thesis: Universitaet Bonn, 2023.

[39] P. Malik, *Linewidth-reduced DBR Laser for Raman Sideband Cooling*,
Master thesis: Universitaet Bonn, 2020.

[40] L. Li, W. Huie, N. Chen, B. DeMarco, and J. P. Covey,
Active Cancellation of Servo-Induced Noise on Stabilized Lasers via Feedforward,
Phys. Rev. Applied **18** (2022) 064005.